Performance Analysis and Low-Complexity Design for XL-MIMO with Near-Field Spatial Non-Stationarities

Kangda Zhi, Cunhua Pan, Hong Ren, Kok Keong Chai, Cheng-Xiang Wang, *Fellow, IEEE*, Robert Schober, *Fellow, IEEE*, Xiaohu You, *Fellow, IEEE*

Abstract

Extremely large-scale multiple-input multiple-output (XL-MIMO) is capable of supporting extremely high system capacities with large numbers of users. In this work, we build a framework for the analysis and low-complexity design of XL-MIMO in the near-field with spatial non-stationarities. Specifically, we first analyze the theoretical performance of discrete-aperture XL-MIMO using an electromagnetic (EM) channel model based on the near-field spherical wave-front. We analytically unveil the impact of the discrete aperture and polarization mismatch on the received power. We also review the amplitude-aware Fraunhofer distance based on the considered EM channel model. Our analytical results indicate that a limited part of the XL-array receives the majority of the signal power in the near-field, which leads to a notion of visibility region (VR) of a user. Thus, we propose a VR detection algorithm and exploit the acquired VR information to design a low-complexity symbol detection scheme. Furthermore, we propose a graph theory-based user partition algorithm, relying on the VR overlap ratio between different users. Partial zero-forcing (PZF) is utilized to eliminate only the interference from users allocated to the same group, which further reduces computational complexity in matrix inversion. Numerical results confirm the correctness of the analytical results and the effectiveness of the proposed algorithms. It reveals that our algorithms approach the performance of conventional whole array (WA)-based designs but with much lower complexity.

Index Terms

K. Zhi and K. K. Chai are with the School of Electronic Engineering and Computer Science at Queen Mary University of London, UK. (e-mail: k.zhi, michael.chai@qmul.ac.uk).

C. Pan, H. Ren, C.-X. Wang, and X. You are with the National Mobile Communications Research Laboratory, Southeast University, China. (cpan, hren, chxwang, xhyu@seu.edu.cn).

R. Schober is with the Institute for Digital Communications, Friedrich-Alexander-University Erlangen-Nürnberg (FAU), Germany (e-mail: robert.schober@fau.de).

Extremely-large-scale MIMO, electromagnetic channel model, visibility region, spatial non-stationarities, near-field communications.

I. INTRODUCTION

To fulfill the various challenging demands on the fifth-generation (5G) and beyond wireless systems, several appealing technologies have been proposed and investigated, including massive multiple-input multiple-output (MIMO) [2]–[5], cell-free [6], small cell [7], millimeter-wave (mmWave) [8], and reconfigurable intelligent surface (RIS) [9]–[12]. Among them, as the evolution of massive MIMO, extremely large-scale MIMO (XL-MIMO) has recently attracted new interest [13], [14]. By mounting several thousands of antennas, XL-MIMO can achieve extremely high spectral efficiency and satisfy the harsh data rate requirements of future wireless systems. XL-MIMO may have large physical dimensions spanning several tens of meters [15]. It is expected to be integrated into large structures such as walls of buildings in mega-city, airports, large shopping malls, and stadiums, and it can serve a large number of users simultaneously.

A classic result for distinguishing the boundary between near and far-field is the Fraunhofer (Rayleigh) distance $d_f = \frac{2D^2}{\lambda}$, where D and λ denote the array aperture and wavelength, respectively [16]. As the array dimension, D, increases, boundary d_f expands, and the users will be easily located in the near-field of the XL-MIMO instead of the far-field. Accordingly, the practical spherical electromagnetic (EM) wave-front can no longer be approximated as planar wave-front. There are multiple differences between near-field and far-field communications. The first one is the nonlinear variation of the phase of the received signal across the whole array. Under the far-field condition, the phase of the array steering vector is approximately linearly scaled for different elements, which makes mathematical analysis tractable. However, this property does not hold in the near-field. Secondly, as the array aperture increases, it is essential to consider the amplitude/pathloss variation across the whole array. This is because the distance between the user and the array center could be significantly different from that between the user and the array edge. Thirdly, in the near-field, the incline angle of the incident wave could vary substantially from the array center to the edge, which results in a variation of the effective projected aperture for different antennas on the array. Therefore, for studying XL-MIMO, it is crucial to consider the practical spherical wave-front and investigate the new features introduced by near-field communications.

Taking into consideration the near-field behavior, XL-MIMO has been studied recently from different perspectives. Focusing on the nonlinear phases of the array steering vector, some work has investigated beam training [17]–[19], channel estimation [20], and multiple-access design [21]. To further accurately model the near-field spherical wave-front, the variation of the amplitude across the array was considered in [22]–[29]. Specifically, the authors of [22] modeled the near-field channel accounting for the variations of the amplitude and incident wave inclination across the whole array. Derived from Maxwell's equations, the authors of [23]–[25] adopted an EM channel model and characterized the EM polarization effect, which accurately describes the physical near-field behavior. These works proved that due to the amplitude attenuation at the array edge, even if the array aperture tends to be infinitely large, the received power of the signal is still limited. However, for tractability, the above contributions [22]–[29] have assumed the array to be spatially continuous, i.e., edge-to-edge antenna deployment with zero antenna spacing or infinitely large numbers of infinitesimal antennas. This structure increases the performance but also causes high fabrication complexity and complicated inter-antenna coupling. By contrast, discrete-aperture XL-MIMO with half-wavelength spacing was studied in [30]–[33]. However, these works did not adopt the EM channel model and therefore the impact of polarization mismatch could not be analyzed.

Another important property of XL-MIMO is spatial non-stationarity [15]. Due to the large array dimension, different parts of the array may have different views of the propagation environment. Besides, due to the variations of amplitude and incident wave inclination, the power of the signal transmitted by a user may be received mainly by a portion of the array, which motivates the notion of user visibility region (VR). The existence of spatial non-stationarities was validated by experimental measurements in [34]. The authors of [35] proposed a near-field channel estimation algorithm for XL-MIMO, which also estimates the mapping between VRs and users. The system performance in the presence of VRs was analyzed in [36]–[39]. By exploiting the feature that users at different locations may have different VRs, novel algorithms were proposed, in terms of low-complexity detectors [40], random access and user scheduling [38], [41], [42], and antenna selection [43]. Nevertheless, large research gaps still exist. Firstly, most of the existing contributions assumed that the VR information was available for algorithm design. A rigorous VR detection algorithm has not been reported yet. Secondly, for tractability, the uniform linear array (ULA) model was widely adopted in these works. For the general uniform planar array (UPA) model, VR detection and the overlapping relationship between the VRs of different users

are more complex and challenging. Finally, most of the existing works assumed that the antennas outside the VR do not receive any signal. In practice, these antennas receive small but not zero power, which complicates algorithm design.

To fill the above research gaps, this work investigates discrete-aperture XL-MIMO based on an EM channel model. We first analyze the impact of the near-field channel on the theoretical performance, which sheds light on the effect of spatial non-stationarities and motivates the design of a VR detection algorithm. Based on the obtained VR information, two low-complexity symbol detection algorithms for XL-MIMO are proposed. The main contributions of this paper are listed as follows.

- Based on the EM channel model, we derive an explicit expression of the signal-to-noise-ratio (SNR) for discrete-aperture XL-MIMO with a single user. We analytically study the near-field characteristics of the SNR, and provide insights into the impact of the discrete aperture and polarization mismatch. We also review the amplitude-aware Fraunhofer distance in the presence of polarization mismatch.

- For multi-user XL-MIMO systems, conventional whole array (WA)-based symbol detectors are proposed and analyzed, including maximum ratio combining (MRC), zero-forcing (ZF), and minimum mean-squared error (MMSE) detection. Next, inspired by the insights drawn from the single-user case, we propose a sub-arrays-based VR detection algorithm based on the explicit received power expressions. Then, a VR-based low-complexity linear symbol detection algorithm is proposed.

- To further exploit the VR information and to reduce complexity, we propose a graph theory-based user partition algorithm. The users whose VRs overlap exceeds a certain threshold are partitioned into one group. Then, the partial ZF (PZF) detector is utilized to only eliminate the interference within the group.

- Simulation results are provided to validate the correctness of analytical results and reveal that the proposed algorithms achieve very similar performance as the conventional WA-based design but with much reduced complexity.

The remainder of this paper is organized as follows. Section II provides the EM channel model for near-field wireless systems. Section III derives the closed-form SNR expression for single-user transmission and analyzes the impact of the discrete aperture and polarization mismatch. Section IV proposes the VR detection algorithm, the user partition algorithm, and two low-
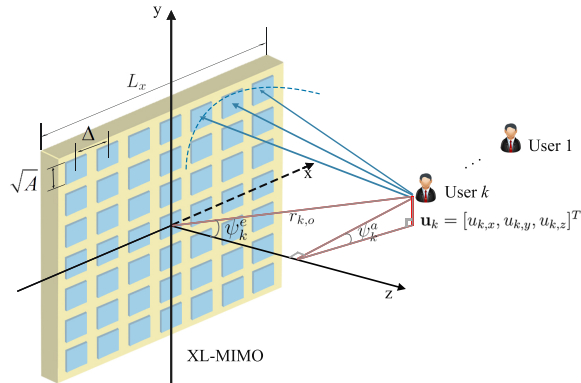
Fig. 1. Illustration of the considered XL-MIMO system.

complexity symbol detection algorithms. Section V presents the numerical results and Section VI concludes the paper.

Notations: Vectors and matrices are denoted by boldface lower case and upper case letters, respectively. The transpose, conjugate transpose, and inverse of matrix $\mathbf{X}$ are denoted by $\mathbf{X}^T$, $\mathbf{X}^H$, and $\mathbf{X}^{-1}$, respectively. $[\mathbf{X}]_{(:,k)}$ denotes the k-th column of matrix $\mathbf{X}$. $\mathcal{O}$ denotes the standard big-O notation. $|\mathcal{B}|$ denotes the cardinality of set $\mathcal{B}$. $\nabla_{\boldsymbol{x}} \times$ denotes the curl operation with respect to $\boldsymbol{x}$.

II. SYSTEM MODEL

As illustrated in Fig. 1, we consider the uplink transmission from K single-antenna users to an XL-MIMO array. The user indices are collected in set $\mathcal{K} = \{1, \ldots, K\}$. For tractability, we establish a coordinate system with the center of the array as the origin. The x-y plane is the plane in which the array lies, and the z-axis is perpendicular to the array. The location of the user $k \in \mathcal{K}$ is denoted by $\mathbf{u}_k = [u_{k,x}, u_{k,y}, u_{k,z}]^T$.

A. XL-MIMO Array Structure

Different from the works considering continuous surfaces or holographic surfaces [22]–[28], a discrete-aperture array model is adopted in this work, where the length of each antenna and the antenna spacing are denoted by $\sqrt{A}$ and Δ, respectively, with $\Delta \geq \sqrt{A}$. The XL-MIMO array has $M = M_x M_y$ antenna elements and the area of each antenna element is A. Define

$\eta = \frac{A}{\Delta^2} \leq 1$ as the array occupation ratio. Considering the (m_x, m_y)-th antenna element, the coordinate of its center is given by $\mathbf{p}_{m_x, m_y} = [m_x \Delta, m_y \Delta, 0]^T$, $m_c \in \mathcal{M}_c$, where

$$\mathcal{M}_c = \{-(M_c - 1)/2, \ldots, (M_c - 1)/2\}, c \in \{x, y\}. \tag{1}$$

The area of the (m_x, m_y)-th antenna element is denoted by $S_{m_x, m_y} = \left[m_x \Delta - \frac{\sqrt{A}}{2}, m_x \Delta + \frac{\sqrt{A}}{2} \right] \times \left[m_y \Delta - \frac{\sqrt{A}}{2}, m_y \Delta + \frac{\sqrt{A}}{2} \right]$. The distance between user k and the center of the (m_x, m_y)-th array element is given by $\left\| \mathbf{r}_{k, m_x, m_y} \right\| = \left\| \mathbf{p}_{m_x, m_x} - \mathbf{u}_k \right\| = \sqrt{(m_x \Delta - u_{k,x})^2 + (m_y \Delta - u_{k,y})^2 + (u_{k,z})^2} \triangleq r_{k, m_x, m_y}$. The distance and the azimuth and elevation angles of arrival (AoAs) from user k to the array center are denoted by $r_{k,o} = \|\mathbf{u}_k\|$ and ψ_k^a and ψ_k^e, respectively.

B. Channel Modeling

The channel from user k to the (m_x, m_y)-th antenna element of the XL-MIMO array is given by

$$h_{k, m_x, m_y} = \sqrt{\xi_{k, m_x, m_y}} e^{-j \frac{2\pi}{\lambda} r_{k, m_x, m_y}}, \tag{2}$$

where ξ_{k, m_x, m_y} and λ are the channel amplitude/pathloss and wavelength, respectively. Then, the channel $\mathbf{h}_k \in \mathbb{C}^{M \times 1}$ from user k to the whole array can be characterized by merging $h_{k, m_x, m_y}, \forall m_x, m_y$, into a vector.

We apply the Dyadic Green's function-based EM channel model for pathloss ξ_{k, m_x, m_y} [23], [24], [44]. This channel model is more practical and allows the characterization of the impact of EM polarization effects. Specifically, consider a point $\mathbf{p} = [p_x, p_y, 0]^T$ located in the area of the (m_x, m_y)-th antenna element, i.e., $\mathbf{p} \in S_{m_x, m_y}$. Based on Maxwell's equations, the electric field of user k satisfies the following inhomogeneous Helmholtz wave equation [23]

$$\left(-\nabla_{\mathbf{u}_k} \times \nabla_{\mathbf{u}_k} \times + k_0^2 \right) \boldsymbol{\mathcal{E}}(\mathbf{u}_k) = j k_0 \kappa \boldsymbol{\mathcal{J}}(\mathbf{u}_k), \tag{3}$$

where $k_0 = \frac{2\pi}{\lambda}$ is the wavenumber, κ is the intrinsic impedance, and $\boldsymbol{\mathcal{E}}(\mathbf{u}_k)$ is the electric field excited by current density $\boldsymbol{\mathcal{J}}(\mathbf{u}_k)$. The inverse map of (3) is given by $\boldsymbol{\mathcal{E}}(\mathbf{p}) = \int \boldsymbol{\mathcal{G}}(\mathbf{p}, \mathbf{u}_k) \boldsymbol{\mathcal{J}}(\mathbf{u}_k) d\mathbf{u}_k$. In EM theory, $\boldsymbol{\mathcal{G}}(\mathbf{p}, \mathbf{u}_k)$ is referred as to the Green function which in the radiating near-field can be approximately expressed as [44]

$$\boldsymbol{\mathcal{G}}(\mathbf{p}, \mathbf{u}_k) \approx \frac{j \kappa e^{j \frac{2\pi}{\lambda} \|\mathbf{r}_k\|}}{2\lambda \|\mathbf{r}_k\|} \left(\mathbf{I}_3 - \hat{\mathbf{r}}_k \hat{\mathbf{r}}_k^H \right), \tag{4}$$

where $\mathbf{r}_k = \mathbf{p} - \mathbf{u}_k = [p_x - u_{k,x}, p_y - u_{k,y}, -u_{k,z}]^T$ and $\hat{\mathbf{r}}_k = \frac{\mathbf{r}_k}{\|\mathbf{r}_k\|}$. For notational simplicity, define $r_k = \|\mathbf{r}_k\|$ and then $\hat{\mathbf{r}}_k = \left[\frac{p_x - u_{k,x}}{r_k}, \frac{p_y - u_{k,y}}{r_k}, \frac{-u_{k,z}}{r_k} \right]^T$. The Green function $\mathcal{G}(\mathbf{p}, \mathbf{u}_k)$ characterizes the EM response at the point $\mathbf{p}$ due to the current source at point $\mathbf{u}_k$. Note that the Green function $\mathcal{G}(\mathbf{p}, \mathbf{u}_k) \in \mathcal{C}^{3 \times 3}$ describes the response between the three polarized directions of the field and the three polarized directions of the source produced by a tripole antenna element. The current of the source can be decomposed orthogonally as $\mathcal{J}(\mathbf{u}_k) = \mathcal{J}_x(\mathbf{u}_k)\hat{\mathbf{e}}_x + \mathcal{J}_y(\mathbf{u}_k)\hat{\mathbf{e}}_y + \mathcal{J}_z(\mathbf{u}_k)\hat{\mathbf{e}}_z$, where $\hat{\mathbf{e}}_c$, $c \in \{x, y, z\}$, are the orthonormal basis vectors, and $\mathcal{J}_c(\mathbf{u}_k)$ denotes the current density in the c polarization direction. As in [23], [24], low-cost uni-polarized antenna elements are considered in this work and the current is assumed to be exited in y-axis direction. Therefore, we have $\mathcal{J}(\mathbf{u}_k) = \mathcal{J}_y(\mathbf{u}_k)\hat{\mathbf{e}}_y$. For unit density $\mathcal{J}_y(\mathbf{u}_k) = 1$, we have $\mathcal{J}(\mathbf{u}_k) = [0, 1, 0]^T$ and

$$
\mathcal{G}(\mathbf{p}, \mathbf{u}_k)\mathcal{J}(\mathbf{u}_k) \triangleq \mathcal{G}_y(\mathbf{r}_k)
$$

$$
= \frac{j\kappa e^{j\frac{2\pi}{\lambda}r_k}}{2\lambda r_k} \left[\frac{(p_x - u_{k,x})(p_y - u_{k,y})}{r_k^2}, 1 - \left(\frac{p_y - u_{k,y}}{r_k} \right)^2, \frac{(-u_{k,z})(p_y - u_{k,y})}{r_k^2} \right]^T. \tag{5}
$$

Based on (5), we can model the pathloss between user k and the (m_x, m_y)-th antenna element as follows

$$
\xi_{k,m_x,m_y} = \int_{S_{m_x,m_x}} \frac{\lambda^2}{\kappa^2\pi} \|\mathcal{G}_y(\mathbf{r}_k)\|^2 \frac{\mathbf{r}_k^T \hat{\mathbf{e}}_z}{\|\mathbf{r}_k\|} d\mathbf{p} \tag{6}
$$

$$
= \int_{S_{m_x,m_x}} \frac{1}{4\pi r_k^2} \frac{u_{k,z}}{r_k} \frac{(p_x - u_{k,x})^2 + u_{k,z}^2}{r_k^2} d\mathbf{p} \tag{7}
$$

$$
\overset{\mathbf{p} \approx \mathbf{p}_{m_x,m_y}}{\approx} \frac{A}{4\pi} \frac{u_{k,z}\left((m_x\Delta - u_{k,x})^2 + u_{k,z}^2 \right)}{\left\{ (m_x\Delta - u_{k,x})^2 + (m_y\Delta - u_{k,y})^2 + u_{k,z}^2 \right\}^{\frac{5}{2}}}, \tag{8}
$$

where (6) includes a normalized factor $\frac{\lambda^2}{\kappa^2\pi}$ and a projection factor $\frac{\mathbf{r}_k^T \hat{\mathbf{e}}_z}{\|\mathbf{r}_k\|}$ which projects the signal to the normal direction to characterize the effective projected aperture due to the incline angle of the incident wave [23], [24]. In (8), since the size of the antenna element is much smaller than distance r_k, all points $\mathbf{p}$ in area S_{m_x,m_x} are approximated by the center point $\mathbf{p}_{m_x,m_y}$. From (7), we can observe that the modeled pathloss is comprised of three components, including the free-space pathloss $\frac{1}{4\pi r_k^2}$, the projection coefficient $\frac{u_{k,z}}{r_k}$, and the polarization mismatch $\frac{(p_x - u_{k,x})^2 + u_{k,z}^2}{r_k^2}$ [24]. Clearly, if the signal is vertically incident, we have $u_{k,x} = u_{k,y} = 0$ and $\frac{u_{k,z}}{r_k} = 1$; if $u_{k,y} = p_y$, then $\frac{(p_x - u_{k,x})^2 + u_{k,z}^2}{r_k^2} = 1$ and (8) simplifies to the case without polarization mismatch

as in [30, (2)]. Thus, the utilized EM channel model is more general and allows us to provide insights into the impact of polarization.

III. SNR ANALYSIS FOR SINGLE-USER SCENARIO

To gain useful insights for system design, in this section, we first focus on a single-user scenario, i.e., $K = 1$. We assume that only user k exists. Our objective is to derive an explicit expression for the SNR and analyze its properties for near-field transmission. The signal received at the XL-MIMO array is expressed as

$$\mathbf{y}_k = \sqrt{p}\mathbf{h}_k x_k + \mathbf{n}, \tag{9}$$

where p is the transmit power, $x_k \sim \mathcal{CN}(0,1)$ is the transmit symbol of user k, and $\mathbf{n} \sim \mathcal{CN}(\mathbf{0}, \sigma^2 \mathbf{I}_M)$. Using an MRC detector, the SNR is calculated as

$$\mathrm{SNR}_k = \frac{p}{\sigma^2}\|\mathbf{h}_k\|^2 = \frac{p}{\sigma^2} \sum_{m_x \in \mathcal{M}_x} \sum_{m_y \in \mathcal{M}_y} \xi_{k,m_x,m_y}, \tag{10}$$

where ξ_{k,m_x,m_y} is given in (8). In the following, we will present an explicit expression of (10) instead of the form with double-sum.

Theorem 1 *Considering channel model (8) and user k with location $\mathbf{u}_k = [u_{k,x}, u_{k,y}, u_{k,z}]^T$, if $u_{k,z} = 0$, we have $\mathrm{SNR}_k = 0$; otherwise, the SNR is given by*

$$\mathrm{SNR}_k = \frac{p}{\sigma^2}\frac{\eta}{6\pi} \left\{ \begin{array}{l} F_k\left(\frac{M_y\Delta}{2} - u_{k,y}, \frac{M_x\Delta}{2} - u_{k,x}\right) + F_k\left(\frac{M_y\Delta}{2} - u_{k,y}, \frac{M_x\Delta}{2} + u_{k,x}\right) \\ +F_k\left(\frac{M_y\Delta}{2} + u_{k,y}, \frac{M_x\Delta}{2} - u_{k,x}\right) + F_k\left(\frac{M_y\Delta}{2} + u_{k,y}, \frac{M_x\Delta}{2} + u_{k,x}\right) \end{array} \right\}, \tag{11}$$

where $F_k(a,b) = \arctan\left(\frac{a}{u_{k,z}} \frac{b}{\sqrt{b^2+a^2+u_{k,z}^2}}\right) + \frac{u_{k,z}}{2} \frac{a}{a^2+u_{k,z}^2} \frac{b}{\sqrt{b^2+a^2+u_{k,z}^2}}.$

Proof: See Appendix A. ∎

For large M, we have $(L_c - M_c\Delta)/L_c \approx 0$, $c \in \{x, y\}$, and therefore the SNR in (11) can be further approximated as

$$\mathrm{SNR}_k = \frac{p}{\sigma^2}\frac{\eta}{6\pi}\left\{ F_k\left(\frac{L_y}{2} - u_{k,y}, \frac{L_x}{2} - u_{k,x}\right) + F_k\left(\frac{L_y}{2} - u_{k,y}, \frac{L_x}{2} + u_{k,x}\right)\right.$$
$$\left. +F_k\left(\frac{L_y}{2} + u_{k,y}, \frac{L_x}{2} - u_{k,x}\right) + F_k\left(\frac{L_y}{2} + u_{k,y}, \frac{L_x}{2} + u_{k,x}\right) \right\}. \tag{12}$$

The SNR in (12) is a function of array lengths L_x, L_y, user location $\mathbf{u}_k$, and array occupation ratio $\eta = \frac{A}{\Delta^2} \leq 1$. Coefficient η shows the difference of discrete-aperture arrays compared with continuous-aperture arrays. The SNR is an increasing function of η since $\eta L_x L_y$ represents the effective array aperture. Next, we aim to analyze the impact of polarization mismatch on the SNR when using a discrete array. Substituting $\frac{\left(p_x - u_{k,x}\right)^2 + u_{k,z}^2}{r_k^2} = 1$ into (7), we can obtain the SNR without polarization mismatch as follows

$$
\text{SNR}_k^{w/o} = \frac{p}{\sigma^2} \frac{\eta}{6\pi} \left\{ \begin{array}{l} F_k^{w/o}\left(\frac{L_y}{2} - u_{k,y}, \frac{L_x}{2} - u_{k,x}\right) + F_k^{w/o}\left(\frac{L_y}{2} + u_{k,y}, \frac{L_x}{2} - u_{k,x}\right) \\ + F_k^{w/o}\left(\frac{L_y}{2} - u_{k,y}, \frac{L_x}{2} + u_{k,x}\right) + F_k^{w/o}\left(\frac{L_y}{2} + u_{k,y}, \frac{L_x}{2} + u_{k,x}\right) \end{array} \right\}, \quad (13)
$$

where $F_k^{w/o}(a,b) = \frac{3}{2}\arctan\left(\frac{ab}{u_{k,z}\sqrt{a^2 + b^2 + u_{k,z}^2}}\right)$. Note that by dividing each term in (13) by $r_{k,o}$ and switching the x-axis and y-axis, this result is identical to that in [30, (12)]. Comparing (12) with (13), we note that function $F_k(a,b)$ is more complex than $F_k^{w/o}(a,b)$, which makes theoretical analysis more challenging. Recall that y-axis polarization direction is assumed. As a result, the polarization mismatch increases with the difference in y-coordinates of the user and the antenna element. Thus, when $L_y \to \infty$ (in the severe near-field), we can show that $\text{SNR}_k \to \frac{2}{3}\text{SNR}_k^{w/o}$, which unveils the possible performance loss caused by polarization mismatch. Besides, for large $u_{k,z}$ (in the far-field), we have $\arctan\left(\frac{a}{u_{k,z}}\frac{b}{\sqrt{b^2+a^2+u_{k,z}^2}}\right) \approx \frac{ab}{u_{k,z}\sqrt{b^2+a^2+u_{k,z}^2}}$ and $\frac{u_{k,z}}{2}\frac{a}{a^2+u_{k,z}^2}\frac{b}{\sqrt{b^2+a^2+u_{k,z}^2}} \approx \frac{ab}{2u_{k,z}\sqrt{b^2+a^2+u_{k,z}^2}}$, which results in $F_k(a,b) \approx F_k^{w/o}(a,b)$ and accordingly $\text{SNR}_k \approx \text{SNR}_k^{w/o} \approx \frac{p}{\sigma^2}\frac{1}{4\pi r_{k,o}^2}MA\cos\psi_k^e$ [30]. This shows that the polarization mismatch plays a more important role in the near-field, and its impact is highly dependent on parameter a, i.e., L_y and $u_{k,y}$.

In addition, it is worth noting that the SNR in (12) can be also understood from the perspective of the 3D angles. Define $\Psi_{k,x} \triangleq \frac{u_{k,x}}{r_{k,o}} = \sin\psi_k^e\cos\psi_k^a$, $\Psi_{k,y} \triangleq \frac{u_{k,y}}{r_{k,o}} = \sin\psi_k^e\sin\psi_k^a$, and $\Psi_{k,z} \triangleq \frac{u_{k,z}}{r_{k,o}} = \cos\psi_k^e$. Then, the SNR can be rewritten as a function of the AoAs and $r_{k,o}$ as follows:

$$
\text{SNR}_k = \frac{p}{\sigma^2}\frac{\eta}{6\pi}\left\{ \begin{array}{l} F_k^A\left(\frac{L_y}{2r_{k,o}} - \Psi_{k,y}, \frac{L_x}{2} - \Psi_{k,x}\right) + F_k^A\left(\frac{L_y}{2r_{k,o}} - \Psi_{k,y}, \frac{L_x}{2} + \Psi_{k,x}\right) \\ + F_k^A\left(\frac{L_y}{2r_{k,o}} + \Psi_{k,y}, \frac{L_x}{2} - \Psi_{k,x}\right) + F_k^A\left(\frac{L_y}{2r_{k,o}} + \Psi_{k,y}, \frac{L_x}{2} + \Psi_{k,x}\right) \end{array} \right\}, \quad (14)
$$

where $F_k^A(a,b) = \arctan\left(\frac{a}{\Psi_{k,z}}\frac{b}{\sqrt{b^2+a^2+\Psi_{k,z}^2}}\right) + \frac{\Psi_{k,z}}{2}\frac{a}{a^2+\Psi_{k,z}^2}\frac{b}{\sqrt{b^2+a^2+\Psi_{k,z}^2}}$.

A. Asymptotic Limit

In massive MIMO systems under far-field conditions and free-space pathloss [2], the SNR in the single-user case is given by $\mathrm{SNR}_k^{\mathrm{far}} = \frac{p}{\sigma^2} \frac{\lambda^2}{(4\pi)^2 r_{k,o}^2} M$, which grows linearly with M to infinity. However, in reality, the received power cannot exceed the transmitted power based on energy conservation. In fact, when $M \to \infty$, the near-field channel model has to be applied and the linear scale in $\mathrm{SNR}_k^{\mathrm{far}}$ no longer holds. Based on the EM near-field channel, when $M \to \infty$, the SNR in (11) converges to

$$\mathrm{SNR}_k \to \frac{p}{\sigma^2} \frac{4\eta}{6\pi} F_k \left(\frac{L_y}{2}, \frac{L_x}{2} \right) \to \frac{p}{\sigma^2} \frac{\eta}{3}. \tag{15}$$

If the polarization mismatch is neglected, the asymptotic SNR becomes

$$\mathrm{SNR}_k^{w/o} \to \frac{p}{\sigma^2} \frac{\eta}{\pi} F_k^{w/o} \left(\frac{L_y}{2}, \frac{L_x}{2} \right) \to \frac{p}{\sigma^2} \frac{\eta}{2}. \tag{16}$$

If the array is assumed to be continuous i.e., $\sqrt{A} = \Delta$, we have

$$\mathrm{SNR}_k^{\mathrm{cont}} \to \frac{p}{\sigma^2} \frac{1}{3}. \tag{17}$$

The results in (15) - (17) provide the practical performance limit for XL-MIMO with an infinitely-large array area. As can be observed, the SNR in (15) is smaller compared with the other two cases in (16) and (17). In (16), at most half of the power can be received by an infinitely large array surface, since it can only capture the power emitting into half of the space. With polarization mismatch, the limit reduces from $1/2$ to $1/3$. This is because as L_y increases, the attenuation of the amplitude from the source to the edge of the array becomes severer in the presence of polarization mismatch, and therefore an additional loss is caused. Besides, for the considered discrete aperture, the asymptotic SNR performance is further limited by array occupation ratio η since it characterizes the effective array area capable of receiving a signal.

The reason why the SNR is limited as $M \to \infty$ can be explained more clearly from the perspective of geometric views. Consider a user located perpendicular to the center of the array,
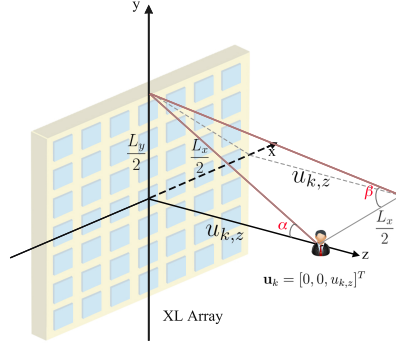
Fig. 2. Geometric interpretation of the SNR.

i.e., $u_{k,x} = u_{k,y} = 0$. Then, the SNR becomes

$$\text{SNR}_k^{\text{p}} = \frac{p}{\sigma^2} \frac{2\eta}{3\pi} \left\{ \arctan \left(\frac{L_y/2}{u_{k,z}} \frac{L_x/2}{\sqrt{\left(\frac{L_x}{2}\right)^2 + \left(\frac{L_y}{2}\right)^2 + u_{k,z}^2}} \right) \right.$$
$$\left. + \frac{1}{2} \frac{u_{k,z}}{\sqrt{\left(\frac{L_y}{2}\right)^2 + u_{k,z}^2}} \frac{L_y/2}{\sqrt{\left(\frac{L_y}{2}\right)^2 + u_{k,z}^2}} \frac{L_x/2}{\sqrt{\left(\frac{L_x}{2}\right)^2 + \left(\frac{L_y}{2}\right)^2 + u_{k,z}^2}} \right\}. \tag{18}$$

Eq. (18) can be rewritten in the form of geometric angles. As illustrated in Fig. 2, we define two angles α and β so that $\tan \alpha = \frac{L_y/2}{u_{k,z}}$ and $\cos \beta = \frac{L_x/2}{\sqrt{\left(\frac{L_x}{2}\right)^2 + \left(\frac{L_y}{2}\right)^2 + u_{k,z}^2}}$. Then, we have

$$\text{SNR}_k^{\text{p}} = \frac{p}{\sigma^2} \frac{2\eta}{3\pi} \left\{ \arctan(\tan \alpha \cos \beta) + \frac{1}{2} \sin \alpha \cos \alpha \cos \beta \right\}. \tag{19}$$

The SNR in (19) is a function of angles α and β. As the aperture of the array increases to infinitely large, however, the angles of view from the user to the array, i.e., α and β, are still limited. Specifically, if $L_x \to \infty$, we have $\beta \to 0$. When $L_y \to \infty$, we have $\alpha, \beta \to \frac{\pi}{2}$. If both L_x and L_y tend to infinity, we have $\alpha \to \frac{\pi}{2}$ and $\beta \to \frac{\pi}{4}$. As a result, the SNR is limited by the angles of view and cannot increase infinitely.

B. XL-ULA

To shed more light on the impact of polarization mismatch, in this section, we consider a simplified case where the XL-UPA degrades to an XL-ULA, i.e., $M_x = 1$ or $M_y = 1$.

Theorem 2 *When $M_y = 1$, the SNR for the XL-ULA simplifies to*

$$\text{SNR}_k^{\text{ULA}} = \frac{p}{\sigma^2} \frac{\eta\Delta}{4\pi} \left\{ F_k^{\text{ULA}} \left(\frac{M_x \Delta}{2} - u_{k,x} \right) + F_k^{\text{ULA}} \left(\frac{M_x \Delta}{2} + u_{k,x} \right) \right\}, \tag{20}$$

where

$$F_k^{\text{ULA}}(a) = \frac{a\left(a^2 u_{k,y}^2 + 3u_{k,z}^2\left(a^2 + u_{k,y}^2 + u_{k,z}^2\right)\right)u_{k,z}}{3\left(u_{k,y}^2 + u_{k,z}^2\right)^2\left(a^2 + u_{k,y}^2 + u_{k,z}^2\right)^{\frac{3}{2}}}. \tag{21}$$

Proof: See Appendix B. ∎

The result in (20) is consistent with [30] only if we have $u_{k,y} = 0$. This is because when $M_y = 1$, the y-coordinate of all antenna elements of the XL-ULA is 0. When the y-coordinate of the user is also $u_{k,y} = 0$, the difference of y-coordinates of the user and all antennas elements is zero, and therefore, there will be no polarization mismatch in pathloss (8). For $M_x \to \infty$, the asymptotic limit of the SNR in (20) is

$$\text{SNR}_k^{\text{ULA}} \overset{M \to \infty}{\Rightarrow} \frac{p}{\sigma^2}\frac{A}{2\pi\Delta}\frac{u_{k,z}\left(u_{k,y}^2 + 3u_{k,z}^2\right)}{3\left(u_{k,y}^2 + u_{k,z}^2\right)^2}. \tag{22}$$

As can be seen, (22) is independent of $u_{k,x}$. This is because as $M_x \to \infty$, the array becomes infinitely long and therefore the x-coordinate of the user does not matter. Furthermore, the asymptotic SNR for the XL-ULA without polarization mismatch is given by

$$\text{SNR}_{k,\text{w/o}}^{\text{ULA}} \overset{M \to \infty}{\Rightarrow} \frac{p}{\sigma^2}\frac{A}{2\pi\Delta}\frac{u_{k,z}}{u_{k,y}^2 + u_{k,z}^2} = \frac{p}{\sigma^2}\frac{A}{2\pi\Delta}\frac{u_{k,z}\left(3u_{k,y}^2 + 3u_{k,z}^2\right)}{3\left(u_{k,y}^2 + u_{k,z}^2\right)^2} \geq \text{SNR}_k^{\text{ULA}}, \tag{23}$$

and the gap between (22) and (23) is

$$D_{\text{SNR}_k} = \text{SNR}_{k,\text{w/o}}^{\text{ULA}} - \text{SNR}_k^{\text{ULA}} = \frac{p}{\sigma^2}\frac{A}{3\pi\Delta}\frac{u_{k,z}u_{k,y}^2}{\left(u_{k,y}^2 + u_{k,z}^2\right)^2}, \tag{24}$$

which first increases and then decreases with respect to $u_{k,y}$. Specifically, we have $D_{\text{SNR}_k} \to 0$ as $u_{k,y} \to 0$ and $u_{k,y} \to \infty$. This is because when $u_{k,y} = 0$, the user possesses the same y-coordinate as the whole ULA, and therefore the polarization mismatch vanishes. As $u_{k,y}$ increases, the difference in the y-coordinate increases, leading to a larger polarization mismatch. For large enough $u_{k,y}$, the user will be located in the far-field and therefore the gap vanishes.

Besides, for $u_{k,x} = u_{k,y} = 0$, we can rewrite the SNR expression in (20) as follows

$$\text{SNR}_k^{\text{ULA}} = \frac{p}{\sigma^2}\frac{\eta\Delta}{2\pi u_{k,z}}\left(\frac{\frac{L_x}{2}}{\sqrt{\left(\frac{L_x}{2}\right)^2 + u_{k,z}^2}}\right)^3 = \frac{p}{\sigma^2}\frac{\eta\Delta}{2\pi u_{k,z}}(\sin\gamma)^3, \tag{25}$$

where γ denotes half of the view angle from the user to the ULA as shown in Fig. 3. Obviously, when $M_y \to \infty$, we have $\gamma \to \frac{\pi}{2}$, and therefore the SNR is limited.
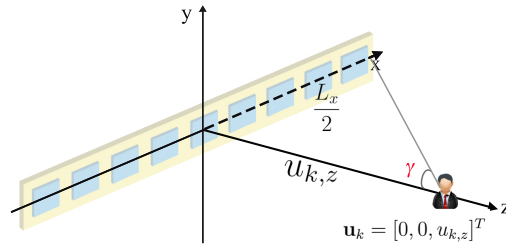
Fig. 3. Geometric interpretation in the case of XL-ULA.

C. Near-Field/Far-Field Boundary

In this section, we revisit the boundary between the near-field and the far-field for the considered discrete array with an EM channel model. A classic result for distinguishing near- and far-field is the Fraunhofer distance [16], [20], [45], i.e., $d_f = \frac{2D^2}{\lambda}$, where D is the array aperture. If the distance is larger than d_f, the phase of the received signal would vary by no more than $\frac{\pi}{8}$ radians across the whole array. In fact, this definition mainly focuses on the variation of the phase between different antenna elements while the amplitude variation of ξ_{k,m_x,m_y} across different antenna elements is ignored. In [30], an amplitude-aware Fraunhofer distance is proposed. Inspired by [30], in this section, we further take the impact of EM polarization into consideration, which is more challenging and leads to a more general result. For brevity, in this section, we assume that M is odd, and the case of even values can be tackled in a similar manner and therefore is omitted here.

Based on the amplitude model of the considered discrete-aperture XL-MIMO array, we quantify the amplitude variation across the whole array as follows

$$\mathrm{v}(\mathbf{u}_k) = \frac{\min_{m_x,m_y} \xi_{k,m_x,m_y}}{\max_{m_x,m_y} \xi_{k,m_x,m_y}}. \tag{26}$$

For $\mathbf{u}_k$ located in the far-field with planar wave-front, we have $\mathrm{v}(\mathbf{u}_k) = 1$. As the user moves closer to the array, the near-field behavior manifests itself, and the variation of the amplitude across the array becomes non-negligible. Therefore, we can define an amplitude variation threshold $\bar{\mathrm{v}}_t \in (0, 1]$, and then determine the near/far-field boundary by finding the set of locations $\tilde{\mathbf{u}}_k$, where $\mathrm{v}(\tilde{\mathbf{u}}_k) = \bar{\mathrm{v}}_t$. Clearly, the field boundary will be a surface comprised of 3D user positions. Based on (8), we can find that the amplitude ξ_{k,m_x,m_y} between user k and the (m_x, m_y)-th antenna element decreases with their y-coordinate difference $|m_y\Delta - u_{k,y}|$ but it is not monotonic of their x-coordinate difference $|m_x\Delta - u_{k,x}|$. This is because when $|m_y\Delta - u_{k,y}|$ increases, both the distance and the polarization mismatch increase. By contrast, when $|m_x\Delta - u_{k,x}|$ increases, the

distance increases but the relative polarization mismatch decreases.

In the following, we derive the explicit values of m_x and m_y which respectively maximize and minimize ξ_{k,m_x,m_y} for given $\mathbf{u}_k$. By defining $s = (m_x\Delta - u_{k,x})^2 + u_{k,z}^2$ and $v = (m_y\Delta - u_{k,y})^2$, we can rewrite ξ_{k,m_x,m_y} in (8) as $f_\xi(s) = \frac{s}{(s+v)^{\frac{5}{2}}}$ with $f'_\xi(s) = (s+v)^{\frac{-7}{2}}(v - \frac{3}{2}s)$. For notational simplicity, define $f_{\text{int}}(a) = \lfloor a + \frac{1}{2} \rfloor$ as the function rounding a to the nearest integer. Define further $f_{\pm x}(a) = \frac{u_{k,x}}{|u_{k,x}|}a$, and $f_{|\min|}(a,b)$, where $f_{|\min|}(a,b) = a$ if $|a| \leq |b|$ and $f_{|\min|}(a,b) = b$ if $|a| > |b|$. Then, based on the range in (1), we can derive the domain of $s \in [s_{\min}, ..., s_{\max}]$, where $s_{\max} = \left(f_{\pm x}\left(\frac{M_x-1}{2}\right)\Delta + u_{k,x}\right)^2 + u_{k,z}^2$ and

$$s_{\min} = \left(\left\{f_{|\min|}\left(f_{\text{int}}\left(\frac{u_{k,x}}{\Delta}\right), f_{\pm x}\left(\frac{M_x-1}{2}\right)\right)\right\}\Delta - u_{k,x}\right)^2 + u_{k,z}^2. \tag{27}$$

By analyzing the properties of $f_\xi(s)$, we obtain the following solutions: to maximize $f_\xi(s)$, we have $\overline{m}_y = f_{|\min|}\left\{f_{\text{int}}\left(\frac{u_{k,y}}{\Delta}\right), f_{\pm y}\left(\frac{M_y-1}{2}\right)\right\}$, $v^* = (\overline{m}_y\Delta - u_{k,y})^2$, and

$$\overline{m}_x = \begin{cases} f_{\text{int}}\left(f_{|\min|}\left\{\frac{\sqrt{\frac{2}{3}v^*-u_{k,z}^2}+u_{k,x}}{\Delta}, \frac{-\sqrt{\frac{2}{3}v^*-u_{k,z}^2}+u_{k,x}}{\Delta}\right\}\right) & \text{if } s_{\min} \leq \frac{2}{3}v^* \leq s_{\max}; \\ f_{|\min|}\left\{f_{\text{int}}\left(\frac{u_{k,x}}{\Delta}\right), f_{\pm x}\left(\frac{M_x}{2}\right)\right\}, & \text{if } \frac{2}{3}v^* < s_{\min}; \\ -f_{\pm x}\left(\frac{M_x-1}{2}\right), & \text{if } \frac{2}{3}v^* > s_{\max}; \end{cases} \tag{28}$$

to minimize $f_\xi(s)$, we have $\underline{m}_y = -f_{\pm y}\left(\frac{M_y}{2}\right)$, $v^* = \left(\underline{m}_y\Delta - u_{k,y}\right)^2$, and

$$\underline{m}_x = \begin{cases} f_{|\min|}\left\{f_{\text{int}}\left(\frac{u_{k,x}}{\Delta}\right), f_{\pm x}\left(\frac{M_x}{2}\right)\right\}, & \text{if } s_{\min} \leq \frac{2}{3}v^* \leq s_{\max}, f_\xi(s_{\min}) \leq f_\xi(s_{\max}); \\ -f_{\pm x}\left(\frac{M_x-1}{2}\right), & \text{if } s_{\min} \leq \frac{2}{3}v^* \leq s_{\max}, f_\xi(s_{\min}) > f_\xi(s_{\max}); \\ f_{|\min|}\left\{f_{\text{int}}\left(\frac{u_{k,x}}{\Delta}\right), f_{\pm x}\left(\frac{M_x}{2}\right)\right\}, & \text{if } \frac{2}{3}v^* > s_{\max}; \\ -f_{\pm x}\left(\frac{M_x-1}{2}\right), & \text{if } \frac{2}{3}v^* < s_{\min}. \end{cases} \tag{29}$$

Based on (28) and (29), we can calculate $\mathrm{v}(\mathbf{u}_k)$ given $\mathbf{u}_k$. Then, to find the $\tilde{\mathbf{u}}_k = [\tilde{u}_{k,x}, \tilde{u}_{k,y}, \tilde{u}_{k,z}]$ on the near/far-field boundary, we can fix $\tilde{u}_{k,x}$ and $\tilde{u}_{k,y}$ and then use a one-dimensional search to find the required value of $\tilde{u}_{k,z}$, which leads to $\mathrm{v}(\tilde{\mathbf{u}}_k) = \bar{\mathrm{v}}_t$.

IV. MULTI-USER SCENARIO

Based on the single-user case, the previous section has shed light on the performance and properties of XL-MIMO in the near field. Next, this section focuses on the general multi-user case and proposes low-complexity symbol detectors by exploiting the near-field properties.

A. Whole Array-Based Design

The signal received by the XL-MIMO array from the K users can be expressed as $\mathbf{y} = \sqrt{p}\mathbf{H}\mathbf{x} + \mathbf{n}$, where $\mathbf{H} = [\mathbf{h}_1, \ldots, \mathbf{h}_K]$ and $\mathbf{x} = [x_1, \ldots, x_K]$. Define $\overline{\mathbf{H}}_k = [\mathbf{H}]_{(:,\mathcal{K}\backslash k)}$ as the matrix obtained by removing the k-th column of $\mathbf{H}$. Then, to detect x_k, linear MRC, ZF, and MMSE detectors for user k are given by [31], [46]

$$\mathbf{a}_{k,\mathrm{MRC}}^H = \frac{\mathbf{h}_k^H}{\|\mathbf{h}_k\|^2}, \tag{30}$$

$$\mathbf{a}_{k,\mathrm{ZF}}^H = \frac{\mathbf{h}_k^H \mathbf{P}_k}{\mathbf{h}_k^H \mathbf{P}_k \mathbf{h}_k}, \mathbf{P}_k = \mathbf{I}_M - \overline{\mathbf{H}}_k \left(\overline{\mathbf{H}}_k^H \overline{\mathbf{H}}_k\right)^{-1} \overline{\mathbf{H}}_k^H, \tag{31}$$

$$\mathbf{a}_{k,\mathrm{MMSE}}^H = \frac{\mathbf{h}_k^H \mathbf{R}_k}{\mathbf{h}_k^H \mathbf{R}_k \mathbf{h}_k}, \mathbf{R}_k = \mathbf{I}_M - \overline{\mathbf{H}}_k \left(\frac{\sigma^2}{p}\mathbf{I}_{K-1} + \overline{\mathbf{H}}_k^H \overline{\mathbf{H}}_k\right)^{-1} \overline{\mathbf{H}}_k^H. \tag{32}$$

Based on the detected symbol $\hat{x}_k = \mathbf{a}_{k,\mathrm{C}}^H \mathbf{y}$, $\mathrm{C} \in \{\mathrm{MRC}, \mathrm{ZF}, \mathrm{MMSE}\}$, the sum user rate is given by $R = \sum_{k=1}^K \log(1 + \mathrm{SINR}_{k,\mathrm{C}})$, where the SINR of user k is expressed as

$$\mathrm{SINR}_{k,\mathrm{MRC}} = \frac{p\|\mathbf{h}_k\|^2}{p\sum_{i=1,i\neq k}^K |\mathbf{h}_k^H \mathbf{h}_i|^2 / \|\mathbf{h}_k\|^2 + \sigma^2}, \tag{33}$$

$$\mathrm{SINR}_{k,\mathrm{ZF}} = \frac{p}{\sigma^2}\mathbf{h}_k^H \mathbf{P}_k \mathbf{h}_k, \tag{34}$$

$$\mathrm{SINR}_{k,\mathrm{MMSE}} = \frac{p}{\sigma^2}\mathbf{h}_k^H \mathbf{R}_k \mathbf{h}_k. \tag{35}$$

For conventional massive MIMO systems with ULA array, the far-field channel of user k can be expressed as $\mathbf{h}_k^{\mathrm{far}} = \xi_k \left[1, e^{-j2\pi\frac{\Delta}{\lambda}\sin\psi_k}, \ldots, e^{-j2\pi\frac{\Delta}{\lambda}(M-1)\sin\psi_k}\right]^T$. As can be seen, different from the considered near-field channel model (2), the amplitudes of different entries of $\mathbf{h}_k^{\mathrm{far}}$ are identical and the phases of different entries of $\mathbf{h}_k^{\mathrm{far}}$ are linearly scaled. Accordingly, the multi-user interference term in (33) can be calculated as [2], [47], [48]

$$\frac{\left|(\mathbf{h}_k^{\mathrm{far}})^H \mathbf{h}_i^{\mathrm{far}}\right|^2}{\left\|\mathbf{h}_k^{\mathrm{far}}\right\|^2} = \frac{\sin^2\left(\pi\frac{\Delta}{\lambda}M(\sin\psi_i - \sin\psi_k)\right)}{M\sin^2\left(\pi\frac{\Delta}{\lambda}(\sin\psi_i - \sin\psi_k)\right)}. \tag{36}$$

Clearly, if user k and user i do not have the same angle, the interference will tend to zero as $M \to \infty$. Therefore, MRC detectors can achieve rather good performance. However, this favorable property no longer holds for near-field channels with spherical waves, where the amplitudes of different entries of $\mathbf{h}_k$ are different and the phases are no longer linearly scaled either, as shown
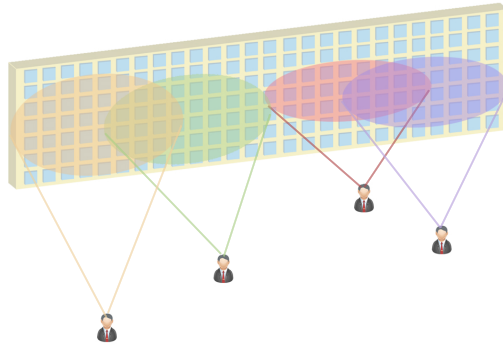
Fig. 4. Illustration of VRs for different users.

in (2). As a result, we have

$$\mathbf{h}_k^H \mathbf{h}_i = \sum_{m_x \in \mathcal{M}_x} \sum_{m_y \in \mathcal{M}_y} \sqrt{\xi_{k,m_x,m_y}^H \xi_{i,m_x,m_y}} e^{j\frac{2\pi}{\lambda}\left(r_{k,m_x,m_y} - r_{i,m_x,m_y}\right)}, \tag{37}$$

which cannot be simplified as a function of the difference of the angles between users k and i. Meanwhile, the denominator term $\|\mathbf{h}_k\|^2$ is finite for large M and therefore the fraction $\left|\mathbf{h}_k^H \mathbf{h}_i\right|^2 / \|\mathbf{h}_k\|^2$ does not tend to zero even if $M \to \infty$. This implies that the low-complexity MRC detector does not work well in XL-MIMO systems in the near field due to the severe interference. To eliminate the interference, ZF or MMSE detectors are needed, which significantly increases the computational complexity due to the required matrix inversion. To tackle this challenge, in the following, we propose low-complexity ZF/MMSE schemes by exploiting the near-field spatial non-stationarity.

B. VR-Based Low-Complexity Design

Section III has analytically shown that due to the amplitude attenuation across the array, the SNR is limited even for an infinitely large array. In other words, a limited part of the array receives a large portion of the signal power, which is referred to as the VR of the user, as illustrated in Fig. 4. The VR can be approximated as a combination of sub-arrays of the XL-MIMO array. Considering that the dimension of the sub-arrays located in the VR of a user could be much smaller than the whole array in the case of large M, we can use the VR of each user to design low-complexity detectors for XL-MIMO.

Algorithm 1 VR Detection

Input: ϖ, $\hat{P}_k = 0$, $\mathcal{B}_k = \emptyset$, SNR_k, $\mathcal{P}_k = \{P_{k,s_x,s_y}, \forall s_x, s_y\}$
Output: $\mathcal{B}_k$

1: **for** $k = 1 : K$ **do**
2:     Sort $\mathcal{P}_k$ using quicksort algorithms; $i = 1$;
3:     **while** $\hat{P}_k \leq \varpi\text{SNR}_k$ **do**
4:         Select the i-th element in $\mathcal{P}_k$ referred as to P_{k,s_x^*,s_y^*};
5:         $\mathcal{B}_k = \{\mathcal{B}_k \cup (s_y^* S_x + s_x^*)\}$;
6:         $\hat{P}_k = \hat{P}_k + P_{k,s_x^*,s_y^*}$; $i = i + 1$;
7:     **end while**
8: **end for**

Lemma 1 *Assume that the XL-MIMO is partitioned into $S = S_x \times S_y$ sub-arrays. For the (s_x, s_y)-th sub-array, where $0 \leq s_x \leq S_x$ and $0 \leq s_y \leq S_y$, the power of signal received from user k is given by*

$$P_{k,s_x,s_y} = \frac{p}{\sigma^2}\frac{\eta}{6\pi}\Big\{F_k\left(f_{s,y,1}\Delta - u_{k,y}, f_{s,x,1}\Delta - u_{k,x}\right) + F_k\left(-f_{s,y,1}\Delta + u_{k,y}, f_{s,x,2}\Delta - u_{k,x}\right)$$
$$+ F_k\left(-f_{s,y,2}\Delta + u_{k,y}, f_{s,x,1}\Delta - u_{k,x}\right) + F_k\left(f_{s,y,2}\Delta - u_{k,y}, f_{s,x,2}\Delta - u_{k,x}\right)\Big\}, \tag{38}$$

where $f_{s,c,1} = \frac{-M_c}{2} + s_c\frac{M_c}{S_c}$, $f_{s,c,2} = \frac{-M_c}{2} + (s_c + 1)\frac{M_c}{S_c}$, $c \in \{x,y\}$.

Proof: For the (s_x, s_y)-th subarray, we can obtain the indices of the antennas as $m_c \in \left\{\frac{-(M_c-1)}{2} + s_c\frac{M_c}{S_c}, \ldots, \frac{-(M_c-1)}{2} + (s_c + 1)\frac{M_c}{S_c} - 1\right\}$, $c \in \{x,y\}$. Then, the proof follows by deriving the sum of the powers across this sub-array using a similar method as in Appendix A.

∎

Based on Lemma 1, the VR of user k can be determined by selecting the sub-arrays contributing to the main portion of the received SNR as ϖSNR_k, where $\varpi \in [0, 1]$ and SNR_k is given in (11). The procedure for detecting VR is shown in Algorithm 1, where step 5 collects the sub-array indices for user k in set $\mathcal{B}_k$. Then, we can only use the sub-arrays belonging to $\mathcal{B}_k$ to detect the symbol of user k, $\forall k$, which helps reduce the computational complexity. Specifically, for user k, we first construct channel $\mathbf{H}_{\text{VR}} \in \mathcal{C}^{(\frac{|\mathcal{B}_k|}{S}M)\times K}$ from the K users to the antenna elements belonging to $\mathcal{B}_k$. Then, the symbol of user k can be detected based on the linear detectors in (33)-(35) by substituting the WA channel matrix $\mathbf{H}$ with VR channel matrix $\mathbf{H}_{\text{VR}}$. Taking VR-based ZF as an example, we have $\mathbf{h}_k^{\text{VR}} = [\mathbf{H}_{\text{VR}}]_{(:,k)}$, $\overline{\mathbf{H}}_k^{\text{VR}} = [\mathbf{H}_{\text{VR}}]_{(:,\mathcal{K}\backslash k)}$, and

the detector of user k is obtained as

$$(\mathbf{a}_{k,\mathrm{ZF}}^{\mathrm{VR}})^H = \frac{(\mathbf{h}_k^{\mathrm{VR}})^H \mathbf{P}_k^{\mathrm{VR}}}{(\mathbf{h}_k^{\mathrm{VR}})^H \mathbf{P}_k^{\mathrm{VR}} \mathbf{h}_k^{\mathrm{VR}}}, \tag{39}$$

where $\mathbf{P}_k^{\mathrm{VR}} = \mathbf{I}_{\frac{|\mathcal{B}_k|}{S}M} - \overline{\mathbf{H}}_k^{\mathrm{VR}} \left((\overline{\mathbf{H}}_k^{\mathrm{VR}})^H \overline{\mathbf{H}}_k^{\mathrm{VR}} \right)^{-1} (\overline{\mathbf{H}}_k^{\mathrm{VR}})^H$.

C. User Partition-Based PZF

Next, we fully exploit the properties of the VRs to further reduce the computational complexity. In the near field, users with different locations may have different VRs, and users whose VRs do not significantly overlap may suffer from low mutual interference. Therefore, we can partition the K users into several groups, where the VRs of users in different groups have low overlap. Then, the users will be mainly affected by the interference caused by the users in their own group. The interference from users in other groups is expected to be weak and can be neglected for detector design. As a result, we propose to utilize the PZF detector [49], [50], which only eliminates intra-group interference and therefore effectively reduces the computational complexity of the required matrix inversion. To begin with, we use the VR information to propose a user partition algorithm based on graph theory.

Definition 1 *[51]: A undirected graph can be denoted as $G = (V, E)$, where V and E are the sets of vertices and edges, respectively. $(u, v) \in E$ means that there is an edge between vertices u and v. The neighborhood of u is $N(u) = \{v \in V | (u, v) \in E\}$ and the degree of u is $d(u) = |N(u)|$. A path D of G is a degree-two path if all vertices of D have edges with each other and have degree two. The maximum independent set of graph G is the maximum vertex set $\mathcal{I} \subseteq V$, in which all vertices have no edge.*

Following Definition 1, we construct an undirected graph $G = (V, E)$ with $V = \{v_1, \ldots, v_K\}$ corresponding to the K users. The edge (v_k, v_i) informs the VR overlap situation between users k and i. Specifically, define $\hat{s}_{\mathrm{ovp}} \in [0, 1]$ as a threshold specifying the maximal overlap ratio between two users' VRs. If $\frac{|\mathcal{B}_k \cap \mathcal{B}_i|}{\min\{|\mathcal{B}_k|, |\mathcal{B}_i|\}} \geq \hat{s}_{\mathrm{ovp}}$, the VR overlap ratio between users k and i is larger than the threshold, and we set edge $(v_k, v_i) \in E$. In order to reduce the matrix inversion complexity while guaranteeing the performance, our target is to partition users into as many as groups possible, where the VRs of different groups have low overlap. To this end, based on the

---

Algorithm 2 User Partition-Based PZF

1: Initialize $\mathcal{I} = \emptyset$
2: Construct graph $G = (V, E)$, $V = \{v_1, \ldots, v_K\}$, $(v_k, v_i) \in E$ if $|\mathcal{B}_k \cap \mathcal{B}_i| \geq \hat{s}_{\text{ovp}} \min\{|\mathcal{B}_k|, |\mathcal{B}_i|\}$
3: Calculate degree $d(v_k)$, $\forall k$; $\mathcal{V}_1 = \{v_k | d(v_k) = 1, \forall k\}$, $\mathcal{V}_2 = \{v_k | d(v_k) = 2, \forall k\}$, $\mathcal{V}_3 = \{v_k | d(v_k) > 2, \forall k\}$
4: **while** $\mathcal{V}_1$ or $\mathcal{V}_2$ or $\mathcal{V}_3 \neq \emptyset$ **do**
5:    **if** $\mathcal{V}_1 \neq \emptyset$ **then**
6:       Delete the neighborhood of $v_k \in \mathcal{V}_1$ from G
7:    **else if** $\mathcal{V}_2 \neq \emptyset$ **then**
8:       Select a vertex $v_k \in \mathcal{V}_2$, find its maximal degree-two path, and delete vertices based on rules in [51, Lemma 4.1]
9:    **else**
10:       Delete the vertex with the largest degree
11:    **end if**
12:    Update the degree for all vertices
13: **end while**
14: $\mathcal{I} = \{v_k | d(v_k) = 0, \forall k\}$
15: **while** $\mathcal{I} \neq \emptyset$ **do**
16:    Select $u \in \mathcal{I}$; construct $\mathcal{L} = \{i | v_i \in \{u, N(u)\} \cap i \in \mathcal{K}\}$
17:    For users i, $i \in \mathcal{L}$, design $\mathbf{a}_{i,\text{PZF}}^H = \frac{\widehat{\mathbf{h}}_i^H \mathbf{L}_i}{\widehat{\mathbf{h}}_i^H \mathbf{L}_i \widehat{\mathbf{h}}_i}$, $\mathbf{L}_i = \mathbf{I}_{|\mathcal{B}_i| \frac{M}{S}} - \widehat{\mathbf{H}}_{\mathcal{L} \setminus i} \left(\widehat{\mathbf{H}}_{\mathcal{L} \setminus i}^H \widehat{\mathbf{H}}_{\mathcal{L} \setminus i} \right)^{-1} \widehat{\mathbf{H}}_{\mathcal{L} \setminus i}^H$,
   where $\widehat{\mathbf{H}}_{\mathcal{L} \setminus i} = \mathbf{H}(\mathcal{M}_i^{\text{VR}}, \mathcal{L} \setminus i)$, $\widehat{\mathbf{h}}_i = \mathbf{H}(\mathcal{M}_i^{\text{VR}}, i)$, and $\mathcal{M}_i^{\text{VR}}$ denotes the antennas indices in the VR of user i
18:    Remove u from $\mathcal{I}$
19: **end while**

---

graph $G = (V, E)$, we solve the following maximum independent set problem:

$$\max |\mathcal{I}|, \text{ s.t. } \mathcal{I} \subseteq V; (u, v) \notin E, \forall u, v \in \mathcal{I}. \tag{40}$$

After solving the maximum independent set problem in (40), we obtain as many as possible vertices in G without edges between each other. In other words, we find as many as possible users with low-overlap VRs. Then, each vertex in $\mathcal{I}$ and its neighborhood form a user group. Based on the user partitioning results, we design the PZF detector to only eliminate the intra-group interference. The detailed procedure is shown in Algorithm 2. Specifically, steps 2 and 3 construct the graph G based on the VRs. Steps 4-14 find the maximum independent set $\mathcal{I}$ of G exploiting a degree-based reduction algorithm with linear complexity $\mathcal{O}(K)$ [51]. Then, each vertex in $\mathcal{I}$ with its neighborhood vertices form one user group $\mathcal{L}$. For each user group, steps 15-19 design the PZF detector by eliminating the interference within the group.

TABLE I
COMPUTATIONAL COMPLEXITY

WA_ZF	$\mathcal{O}\left\{M^2K^2 + K^4\right\}$
VR_ZF	$\mathcal{O}\{(|\widetilde{\mathcal{B}}|/S)^2 M^2 K^2 + K^4 + KS\log(S)\}$
UP_PZF	$\mathcal{O}\{(|\widetilde{\mathcal{B}}|/S)^2 M^2 K^2/|\widetilde{\mathcal{I}}| + K^4/|\widetilde{\mathcal{I}}|^3 + KS\log(S)\}$

D. Complexity Analysis

For brevity, only the complexity of ZF is analyzed since MMSE and ZF have the same asymptotic complexity. We refer to the three algorithms as whole array-based ZF (WA_LD), VR-based ZF (VR_LD), and user partitioning-based PZF (UP_PZF). The results are presented in Table I. For tractability, we consider an ideal case where the VR of each user includes the same number of sub-arrays, i.e., $|\mathcal{B}_k| = |\widetilde{\mathcal{B}}|$, $\forall k$. Then, the number of antennas in the VR of each user reduces from M to $\frac{|\widetilde{\mathcal{B}}|}{S}M$. We also ideally assume that for the user partitioning algorithm, K users are divided uniformly into $|\widetilde{\mathcal{I}}|$ groups. Therefore, the matrix dimension for the inversion operation in the PZF scheme reduces from K to $K/|\widetilde{\mathcal{I}}|$. Table I reveals that the proposed algorithms can significantly reduce the complexity when $|\widetilde{\mathcal{B}}|/S$ is small and when $|\widetilde{\mathcal{I}}|$ is large.

V. SIMULATION RESULTS

In this section, we provide numerical results for validating our analytical conclusions and providing insight into the performance of XL-MIMO systems. Following the literature [30]–[33], we set $\Delta = \frac{\lambda}{2} = 0.0628$ m, $\frac{p}{\sigma^2} = 90$ dB, $A = \frac{\lambda^2}{4\pi}$, and $\bar{v}_t = 0.9$.

A. Single-User Case

To begin with, the single-user case is considered. Fig. 5 depicts the SNR performance as the aperture of the XL-UPA grows infinitely large. It can be seen that different from the far-field-based result which increases linearly with M, the near-field-based SNR first increases but then saturates to a limit as $M \to \infty$. Furthermore, the proposed model, which takes into consideration both the discrete aperture and polarization mismatch, characterizes the actual performance with additional loss. Besides, it can be seen that the SNR in (10) which includes a double sum is well approximated by the derived explicit result.
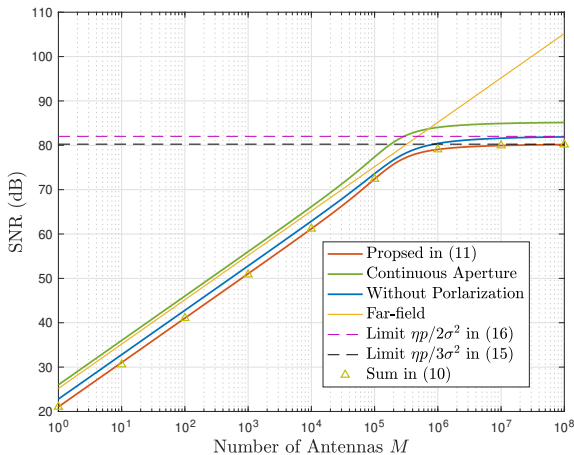
Fig. 5. SNR versus M for XL-UPA, $\mathbf{u}_k = [10, 10, 10]$, $M_x = M_y = \sqrt{M}$.
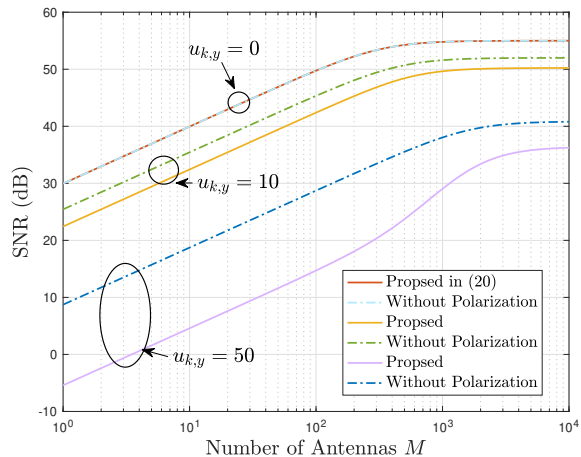

Fig. 6. SNR versus M for XL-ULA, $\mathbf{u}_k = [0, u_{k,y}, 10]$, $M_x = M$, $M_y = 1$.

In Fig. 6, the asymptotic SNR of XL-ULA is studied. A similar tendency as in Fig. 5 is observed. However, the number of antennas needed for the SNR growth rate to slow down is much smaller than that in Fig. 5. The SNR of ULA becomes saturated for almost 10^3 antenna elements while the required number of antenna elements for UPA is 10^6. This is because given M, the ULA has a much larger dimension than UPA and therefore the variations of the amplitude, the signal incline angles, and the polarization mismatch across the whole array are more apparent. As a result, the near-field behavior becomes more obvious for the ULA with a given M. This phenomenon can also be understood via the geometric figures in Fig. 2 and 3. As M increases, the enlarging of view of angles γ is easier to saturate for ULA than angles α and β for UPA. Furthermore, it can be observed that the SNR gap between the proposed EM model and the model without polarization mismatch enlarges as the y-coordinate of the user increases. This phenomenon agrees with our analytical result (24) since the polarization mismatch is proportional to the difference in the y-coordinate between the user and the received antenna. As a result, as $u_{k,y}$ increases, the performance loss caused by polarization mismatch increases, which enlarges the gap.

In Fig. 7, the amplitude-aware Fraunhofer distance is re-examined after taking into consideration the impact of polarization mismatch. We also present results for the case when the polarization mismatch and both the polarization mismatch and the angle projection are neglected, respectively. Different from the classic phase-aware Fraunhofer distance which gives a semicircle, the three amplitude-aware Fraunhofer distances shrink as the user moves towards the center of the array (i.e., as x-coordinate $\to 0$). This is because the variation of the amplitude from the
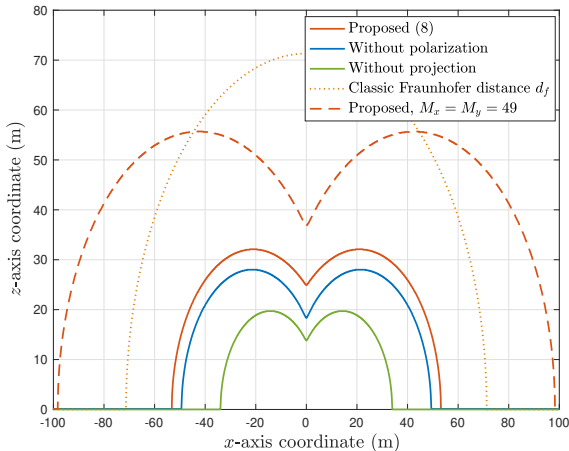
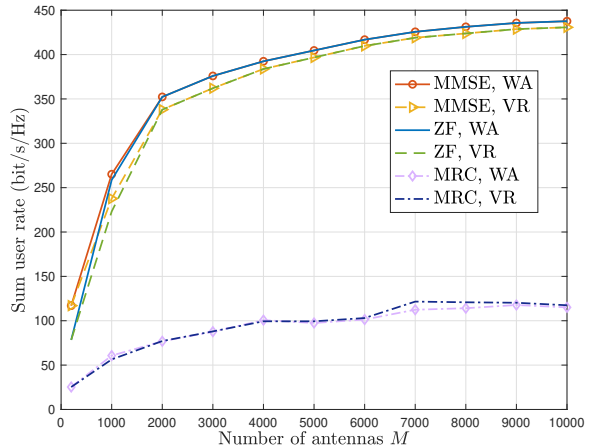Fig. 7. Field boundaries at $u_{k,y} = 0$, $M_x = M_y = 25$.

Fig. 8. Comparison of WA and VR-based design.

center to the edge of the array is smaller than that from one edge to the other edge of the array. For a milder amplitude variation, the near-field region is reduced. Besides, as can be observed, the considered EM channel model results in a larger Fraunhofer distance since the polarization mismatch further aggravates the amplitude variation across the array. Furthermore, the Fraunhofer distance increases with M due to the larger array dimension and the more apparent near-field behavior.

B. Multi-User Case

The previous subsection illustrated the impact of near-field spatial non-stationarities, which inspired the proposed low-complexity design for multi-user scenarios. In this section, numerical results are presented to illustrate the effectiveness of the proposed algorithms. Unless stated otherwise, we assume that $M = 10^4$, $M_y = 10$, $S_y = 2$, $M_x/S_x = 10$, $\varpi = 0.8$, and $\hat{s}_{\mathrm{ovp}} = 0.6$. $K = 20$ users are randomly distributed in the region of $[-25, 25] \times [2, 12]$.

In Fig. 8, we compare the whole array (WA)-based design with the proposed VR-based design. The WA-based MMSE, ZF, and MRC detection are carried out based on (30)-(32), while the VR-based design is conducted as (39). It can be seen that for both the WA and VR-based cases, the sum user rates for the MMSE and ZF detectors coincide for large M and are much higher than that for MRC. This is because in near-field scenarios with spherical wave-fronts, the favorable interference condition in (36) no longer holds, which deteriorates to (37) as a function of distances and angles. Therefore, considering that the computational complexity of ZF and MMSE is much higher than that of MRC, it is necessary to employ low-complexity detectors in
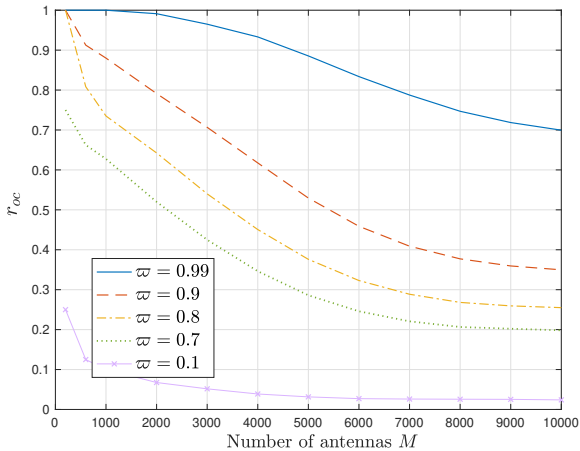
Fig. 9. Ratio of average number of antennas employed by VR-based design.
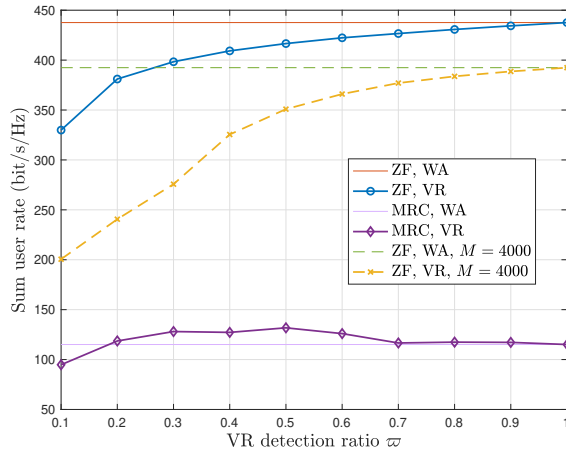
Fig. 10. Sum user rate under different ϖ, where $M = 10^4$.

XL-MIMO systems. From Fig. 8, it can be observed that the proposed VR-based low-complexity MMSE and ZF detectors perform very close to the WA-based design, especially in the context of large M. This is because for XL-MIMO with the large physical dimension, the variations of the amplitude, incline angle, and polarization mismatch across the array are apparent. As a result, the majority of the signal power is received on a limited portion of the array. In other words, the user will "see" only a part of the array (i.e., the VR). If the VRs are accurately detected, it is expected that the proposed VR-based algorithms can achieve a performance very similar to that of the WA-based design. Meanwhile, for large M, the portion of the array that contributes marginal received power grows. Thus, for a given ratio ϖ, the VR detection algorithm (Algorithm 1) is more efficient in finding the most relevant sub-arrays, which leads to a smaller performance gap between the VR and WA-based designs.

Intuitively, the proposed VR-based design aims to achieve a trade-off between performance and complexity, which can be adjusted by the VR detection ratio ϖ as shown in Algorithm 1. To quantify the complexity, the ratio of the average number of antennas employed by VR-based design to the number of antennas employed by the WA-based design is defined as $r_{oc} = \frac{1}{K} \sum_{k \in \mathcal{K}} \frac{|\mathcal{B}_k|}{S}$. Clearly, we have $r_{oc} = 1$ for the WA-based design. Next, Figs. 9 and 10 illustrate the trade-off between performance and the complexity when using VR-based detectors.

From Fig. 9, we observe that ratio r_{oc} is an increasing function of the VR detection ratio ϖ, which implies that the number of antennas considered for the computation of the VR-based detectors increases with ϖ. This is because the VR is defined as the set of sub-arrays that

contribute a fraction of ϖ to the whole received power. The larger ϖ is, the more sub-arrays are included in the VR. Besides, as can be seen, r_{oc} is a decreasing function of M. For small M, r_{oc} could even approach 1. This phenomenon actually underscores the motivation for proposing the VR-based design for XL-MIMO. Specifically, as the number of antennas grows, the physical size of the array becomes large, and the portion of the array that receives marginal power increases. In this context, it is inefficient to use the whole array to compute the symbol detectors, since most of the power is concentrated in a small portion of the array. By contrast, when M is small, all sub-arrays may receive non-negligible power and therefore r_{oc} approaches one. It can be seen from Fig. 9 that for an XL-MIMO array with $M = 10^4$, 25% of the antennas receive 80% power (i.e., $\varpi = 0.8$), which can be exploited to significantly reduce the computational complexity in VR-based detection.

Fig. 10 reveals the performance loss caused by the reduction of the complexity. As can be seen, for ZF detection, the performance loss is small for moderate values of ϖ, but performance deteriorates when ϖ is small. This is because as shown in Fig. 9, when $M = 10^4$, less than 5% of the antennas contribute 10% of the power, 20% of the antennas contribute 70% of the power, and 70% of the antennas contribute 99% of the power. As a result, for a moderate value of ϖ, we can find sub-arrays that receive the main part of the power in the VR but also with a small number of antennas, which leads to a good performance at low complexity. In other words, a moderate value of ϖ can realize a good trade-off between performance and complexity. Besides, it can be observed that when ϖ is small, the data rate degradation is severer under small M. This is because for arrays with small sizes, the spatial non-stationarity effect is weaker, and therefore more sub-arrays have to be used to receive sufficient power and to realize a good performance. Furthermore, for MRC, the VR-based design may perform better than the WA-based design. The reason is that for VR-based MRC, the multi-user interference will be small when the VRs of the users have less overlap.

In Figs. 11 and 12, we investigate the performance of the proposed user partitioning-based PZF algorithm. Fig. 11 shows that the proposed PZF detector can achieve almost the same performance as the VR-based detectors for any value of M and for different values of K. This is because for the VR-based detectors, the users mainly suffer from the interference from other users having VRs with large overlap. Therefore, it is reasonable to partition users into different groups based on the VR information, and then eliminate only the intra-group interference. Meanwhile, for the PZF detectors, a part of the channel degrees-of-freedom (DoFs) are used for interference
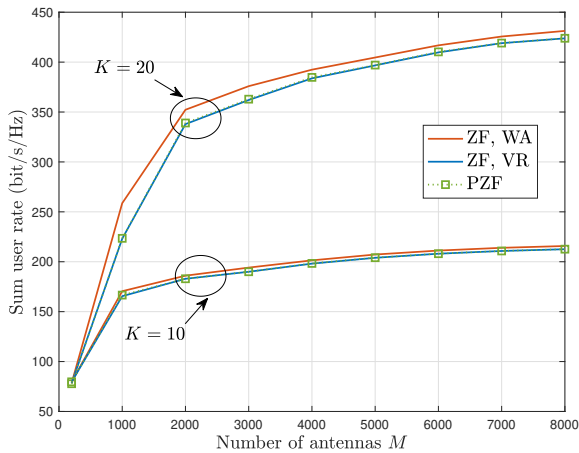
Fig. 11. Comparison of VR-based and PZF-based design, $\varpi = 0.8$, $\hat{s}_{\mathrm{ovp}} = 0.6$.
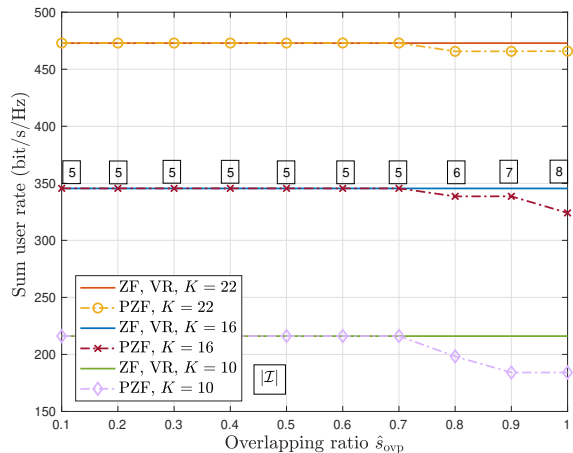
Fig. 12. Sum user rate versus the threshold of VR overlapping ratio $\hat{s}_{\mathrm{ovp}}$.

nulling while the remaining DoFs are used to enhance the desired signal, which is beneficial for performance improvement.

The PZF detectors exploit user partitioning which is determined by VR overlap threshold $\hat{s}_{\mathrm{ovp}}$, as specified in Algorithm 2. In Fig. 12, we observe that the PZF algorithm only causes a performance loss for large $\hat{s}_{\mathrm{ovp}}$. This is because as $\hat{s}_{\mathrm{ovp}}$ increases, the condition that adds an edge between two vertices becomes stricter, and thus the size of the independent set $|\mathcal{I}|$ could grow. In other words, for large $\hat{s}_{\mathrm{ovp}}$, the users significantly interfering with each other may not have edges connecting them, and they could be partitioned into different groups, and therefore the dominant interference may not be eliminated clearly by the intra-group PZF algorithm. With proper user partitioning (moderate $\hat{s}_{\mathrm{ovp}}$), the PZF algorithm can effectively tackle the dominant interference and therefore cause negligible performance loss at low complexity. Besides, it can be seen that the proposed PZF algorithm performs better for larger K.

Fig. 13 shows the computational complexity of WA-based ZF, VR-based ZF, and user partition-based PZF detection. Following Table I, the complexity is computed based on the actual VR detection and user partitioning results in MATLAB. As can be seen, the complexity of the conventional WA-based design has a polynomial growth rate, which is not favorable considering the large number of antennas typically for XL-MIMO systems. However, by effectively exploiting the near-field spatial non-stationarities, the two proposed algorithms achieve much lower complexities. VR-based ZF detection has a complexity that increases sub-linearly with the
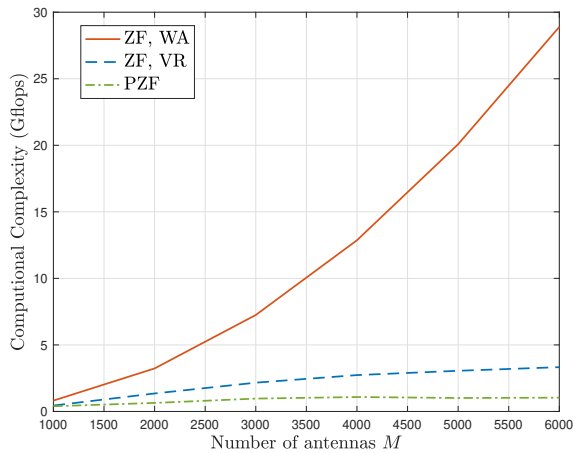
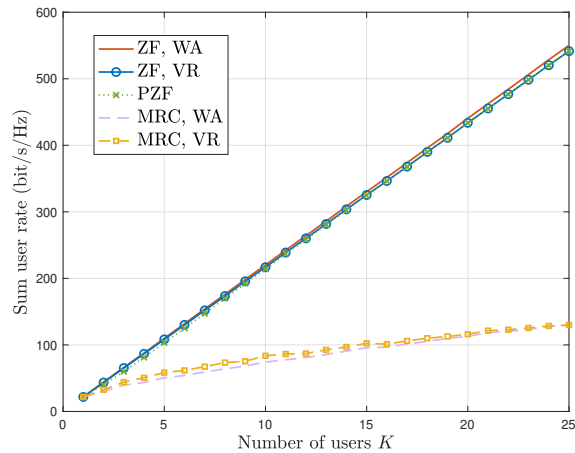Fig. 13. Comparison of the computational complexity.

Fig. 14. Sum user rate versus the number of users.

number of antennas, and the complexity of user partitioning-based PZF practically saturates for large M. The reasons for this are two-fold. On the one hand, the growth rate of the number of antennas in the VRs is much lower than M. As shown in Fig. 9, given $\varpi = 0.7$, as M increases from 10^3 to 10^4, the average number of antennas in the VRs only increases from 600 to 2000. On the other hand, for large M, the physical size of the array grows, and therefore, the VRs of different users become more separated on average. Accordingly, users can be divided into more groups, and then the computational complexity needed for PZF to eliminate the intra-group interference reduces.

Finally, Fig. 14 illustrates the motivation and benefits of employing XL-MIMO. It can be seen that XL-MIMO has the capability to support a large number of users with extremely-high throughput. The sum user rate is nearly linear increasing in terms of the number of users for WA-based ZF, VR-based ZF, and PZF detectors. Meanwhile, the proposed low-complexity VR-based and PZF detection algorithms achieve a performance very similar to the WA-based detection for all considered values of K. However, as has been shown in Fig. 13, the proposed algorithms have much lower computational complexity. Therefore, Fig. 14 demonstrates the ability of the proposed VR-based and user partitioning-based PZF algorithms to support extremely-high capacities in XL-MIMO systems at comparatively low complexity. Fig. 14 also confirms the effectiveness and necessity of exploiting spatial non-stationarities when using the XL-MIMO.

VI. CONCLUSION

In this work, we investigated the performance of XL-MIMO based on the EM channel model with near-field spatial non-stationarities. We derived the explicit expression for the SNR for the single-user case, which provided useful insights regarding the impact of the discrete aperture and polarization mismatch. We also studied the Fraunhofer distance under the proposed EM channel model. Then, we exploited the near-field characteristics to develop VR-based low-complexity linear detectors. We also provided a graph theory-based user partition algorithm, based on which PZF was used to further reduce the computational complexity. Simulation results validated the effectiveness of the proposed two low-complexity algorithms.

APPENDIX A

Define $\epsilon = \frac{\Delta}{r_{k,o}}$, where $r_{k,o} = \|\mathbf{u}_k\|$ is the distance between user k and the origin. Substituting ξ_{k,m_x,m_y} in (10) with (8), we have

$$\mathrm{SNR}_k = \frac{p}{\sigma^2} \sum_{m_y \in \mathcal{M}_y} \sum_{m_x \in \mathcal{M}_x} \frac{A}{4\pi} \frac{u_{k,z}\left((m_x\Delta - u_{k,x})^2 + u_{k,z}^2\right)}{\left\{(m_x\Delta - u_{k,x})^2 + (m_y\Delta - u_{k,y})^2 + u_{k,z}^2\right\}^{\frac{5}{2}}} \tag{41}$$

$$= \frac{p}{\sigma^2} \sum_{m_y \in \mathcal{M}_y} \sum_{m_x \in \mathcal{M}_x} \frac{\eta\epsilon^2}{4\pi} \frac{\bar{u}_{k,z}\left((m_x\epsilon - \bar{u}_{k,x})^2 + \bar{u}_{k,z}^2\right)}{\left\{(m_x\epsilon - \bar{u}_{k,x})^2 + (m_y\epsilon - \bar{u}_{k,y})^2 + \bar{u}_{k,z}^2\right\}^{\frac{5}{2}}}, \tag{42}$$

where $\bar{u}_{k,c} = \frac{u_{k,c}}{r_{k,o}}$, $c \in \{x, y, z\}$. Since $r_{k,o} \gg \Delta$, we have $\epsilon \ll 1$. Then, we have

$$\mathrm{SNR}_k \overset{(a)}{=} \frac{p}{\sigma^2} \frac{\eta\epsilon^2}{4\pi} \sum_{\hat{y}=\frac{-(M_y-1)\epsilon}{2}}^{\frac{(M_y-1)\epsilon}{2}} \sum_{\hat{x}=\frac{-(M_x-1)\epsilon}{2}}^{\frac{(M_x-1)\epsilon}{2}} \frac{\bar{u}_{k,z}\left((\hat{x} - \bar{u}_{k,x})^2 + \bar{u}_{k,z}^2\right)}{\left\{(\hat{x} - \bar{u}_{k,x})^2 + (\hat{y} - \bar{u}_{k,y})^2 + \bar{u}_{k,z}^2\right\}^{\frac{5}{2}}} \tag{43}$$

$$\overset{(b)}{\approx} \frac{p}{\sigma^2} \frac{\eta\epsilon^2}{4\pi} \frac{1}{\epsilon^2} \int_{\frac{-(M_y-1)\epsilon}{2} - \frac{\epsilon}{2}}^{\frac{(M_y-1)\epsilon}{2} + \frac{\epsilon}{2}} \int_{\frac{-(M_x-1)\epsilon}{2} - \frac{\epsilon}{2}}^{\frac{(M_x-1)\epsilon}{2} + \frac{\epsilon}{2}} \frac{\bar{u}_{k,z}\left((\hat{x} - \bar{u}_{k,x})^2 + \bar{u}_{k,z}^2\right)}{\left\{(\hat{x} - \bar{u}_{k,x})^2 + (\hat{y} - \bar{u}_{k,y})^2 + \bar{u}_{k,z}^2\right\}^{\frac{5}{2}}} d\hat{x}d\hat{y} \tag{44}$$

$$\overset{(c)}{=} \frac{p}{\sigma^2} \frac{\eta\epsilon^2}{4\pi} \frac{\bar{u}_{k,z}}{\epsilon^2} \int_{\frac{-M_x\epsilon}{2} - \bar{u}_{k,x}}^{\frac{M_x\epsilon}{2} - \bar{u}_{k,x}} \int_{\frac{-M_y\epsilon}{2} - \bar{u}_{k,y}}^{\frac{M_y\epsilon}{2} - \bar{u}_{k,y}} \frac{\left(x^2 + \bar{u}_{k,z}^2\right)}{\left\{x^2 + y^2 + \bar{u}_{k,z}^2\right\}^{\frac{5}{2}}} dydx \tag{45}$$

where the change of variables $\hat{x} = m_x\epsilon$ and $\hat{y} = m_y\epsilon$ is applied in (a). In (b), since $\epsilon \ll 1$, all variables within domain $[\hat{x} \pm \frac{\epsilon}{2}] \times [\hat{y} \pm \frac{\epsilon}{2}]$ of area ϵ^2 approximately achieve the same objective function value as the center point $(\hat{x}, \hat{y})$. Then, the double sum is approximated by a double integral divided by $\frac{1}{\epsilon^2}$. The change of variables $x = \hat{x} - \bar{u}_{k,x}, y = \hat{y} - \bar{u}_{k,y}$ is used in (c). The

proof can be completed by first solving the integral in (45) with respect to y based on [52, 2.271.6] and then solving the integral with respect to x using [52, (2.271.5)] and [52, (2.284)].

APPENDIX B

For the case of $M_y = 1$, we have

$$
\begin{aligned}
\text{SNR}_k &= \frac{p}{\sigma^2} \frac{\eta \epsilon^2}{4\pi} \sum_{m_x = \frac{-(M_x-1)}{2}}^{\frac{(M_x-1)}{2}} \frac{\bar{u}_{k,z}\left((m_x\epsilon - \bar{u}_{k,x})^2 + \bar{u}_{k,z}^2\right)}{\left\{(m_x\epsilon - \bar{u}_{k,x})^2 + \bar{u}_{k,y}^2 + \bar{u}_{k,z}^2\right\}^{\frac{5}{2}}} \\
&\approx \frac{p}{\sigma^2} \frac{\eta \epsilon^2}{4\pi} \frac{1}{\epsilon} \int_{\frac{-M_x\epsilon}{2}}^{\frac{M_x\epsilon}{2}} \frac{\bar{u}_{k,z}\left((\hat{x} - \bar{u}_{k,x})^2 + \bar{u}_{k,z}^2\right)}{\left\{(\hat{x} - \bar{u}_{k,x})^2 + \bar{u}_{k,y}^2 + \bar{u}_{k,z}^2\right\}^{\frac{5}{2}}} d\hat{x} \\
&= \frac{p}{\sigma^2} \frac{\eta \epsilon^2}{4\pi} \frac{1}{\epsilon} \bar{u}_{k,z} \int_{\frac{-M_x\epsilon}{2} - \bar{u}_{k,x}}^{\frac{M_x\epsilon}{2} - \bar{u}_{k,x}} \frac{1}{\left\{x^2 + \bar{u}_{k,y}^2 + \bar{u}_{k,z}^2\right\}^{\frac{3}{2}}} - \frac{\bar{u}_{k,y}^2}{\left\{x^2 + \bar{u}_{k,y}^2 + \bar{u}_{k,z}^2\right\}^{\frac{5}{2}}} dx.
\end{aligned}
\tag{46}
$$

Utilizing [52, (2.271.5)] and [52, (2.271.6)], we can complete the proof after some algebraic operations.

REFERENCES

[1] K. Zhi, C. Pan, T. Wu, H. Ren, and K. K. Chai, "Analysis of XL-array with near-field EM channels," submitted to EUSIPCO 2023.

[2] E. Björnson, J. Hoydis, and L. Sanguinetti, "Massive MIMO networks: Spectral, energy, and hardware efficiency," *Found. Trends Signal Process.*, vol. 11, no. 3-4, pp. 154–655, Nov. 2017.

[3] E. Björnson, M. Matthaiou, and M. Debbah, "Massive MIMO with non-ideal arbitrary arrays: Hardware scaling laws and circuit-aware design," *IEEE Trans. Wireless Commun.*, vol. 14, no. 8, pp. 4353–4368, Aug. 2015.

[4] J. Zhang, E. Björnson, M. Matthaiou, D. W. K. Ng, H. Yang, and D. J. Love, "Prospective multiple antenna technologies for beyond 5G," *IEEE J. Sel. Areas Commun.*, vol. 38, no. 8, pp. 1637–1660, Aug. 2020.

[5] K. Zhi, C. Pan, G. Zhou, H. Ren, M. Elkashlan, and R. Schober, "Is RIS-aided massive MIMO promising with ZF detectors and imperfect CSI?" *IEEE J. Sel. Areas Commun.*, vol. 40, no. 10, pp. 3010–3026, Oct. 2022.

[6] E. Björnson and L. Sanguinetti, "Scalable cell-free massive MIMO systems," *IEEE Trans. Communications*, vol. 68, no. 7, pp. 4247–4261, Jul. 2020.

[7] G. Chen, L. Qiu, and Y. Li, "Stochastic geometry analysis of coordinated beamforming small cell networks with CSI delay," *IEEE Commun. Lett.*, vol. 22, no. 5, pp. 1066–1069, May 2018.

[8] R. W. Heath, N. González-Prelcic, S. Rangan, W. Roh, and A. M. Sayeed, "An overview of signal processing techniques for millimeter wave MIMO systems," *IEEE J. Sel. Topics Signal Process.*, vol. 10, Apr. 2016.

[9] C. Pan *et al.*, "Intelligent reflecting surface aided MIMO broadcasting for simultaneous wireless information and power transfer," *IEEE J. Sel. Areas Commun.*, vol. 38, no. 8, pp. 1719–1734, Aug. 2020.

[10] C. Huang *et al.*, "Reconfigurable intelligent surfaces for energy efficiency in wireless communication," *IEEE Trans. Wireless Commun.*, vol. 18, no. 8, pp. 4157–4170, Aug. 2019.

[11] C. Pan *et al.*, "Multicell MIMO communications relying on intelligent reflecting surfaces," *IEEE Trans. Wireless Commun.*, vol. 19, no. 8, pp. 5218–5233, Aug. 2020.

[12] G. Chen, Q. Wu, C. He, W. Chen, J. Tang, and S. Jin, "Active IRS aided multiple access for energy-constrained IoT systems," *IEEE Trans. Wireless Commun.*, vol. 22, no. 3, pp. 1677–1694, Mar. 2023.

[13] E. Björnson, L. Sanguinetti, H. Wymeersch, J. Hoydis, and T. L. Marzetta, "Massive MIMO is a reality—what is next?: Five promising research directions for antenna arrays," *Digital Signal Process.*, vol. 94, pp. 3–20, Nov. 2019.

[14] Z. Wang, J. Zhang, H. Du, W. E. Sha, B. Ai, D. Niyato, and M. Debbah, "Extremely large-scale MIMO: Fundamentals, challenges, solutions, and future directions," *arXiv preprint arXiv:2209.12131*, 2022.

[15] E. De Carvalho, A. Ali, A. Amiri, M. Angjelichinoski, and R. W. Heath, "Non-stationarities in extra-large-scale massive MIMO," *IEEE Wireless Commun.*, vol. 27, no. 4, pp. 74–80, Aug. 2020.

[16] K. T. Selvan and R. Janaswamy, "Fraunhofer and fresnel distances: Unified derivation for aperture antennas." *IEEE Antennas Propag. Mag.,*, vol. 59, no. 4, pp. 12–15, Aug. 2017.

[17] M. Cui, L. Dai, Z. Wang, S. Zhou, and N. Ge, "Near-field rainbow: Wideband beam training for XL-MIMO," *IEEE Trans. Wireless Commun.*, early access, 2022.

[18] W. Liu, H. Ren, C. Pan, and J. Wang, "Deep learning based beam training for extremely large-scale massive MIMO in near-field domain," *IEEE Commun. Lett.*, vol. 27, no. 1, pp. 170–174, Jan. 2023.

[19] Y. Zhang, X. Wu, and C. You, "Fast near-field beam training for extremely large-scale array," *IEEE Wireless Commun. Lett.*, vol. 11, no. 12, pp. 2625–2629, Dec. 2022.

[20] M. Cui and L. Dai, "Channel estimation for extremely large-scale MIMO: Far-field or near-field?" *IEEE Trans. Commun.*, vol. 70, no. 4, pp. 2663–2677, Jan. 2022.

[21] Z. Wu, M. Cui, and L. Dai, "Multiple access for near-field communications: SDMA or LDMA?" *arXiv preprint arXiv:2208.06349*, 2022.

[22] S. Hu, F. Rusek, and O. Edfors, "Beyond massive MIMO: The potential of data transmission with large intelligent surfaces," *IEEE Trans. Signal Process.*, vol. 66, no. 10, pp. 2746–2758, May 2018.

[23] D. Dardari, "Communicating with large intelligent surfaces: Fundamental limits and models," *IEEE J. Sel. Areas Commun.*, vol. 38, no. 11, pp. 2526–2537, Nov. 2020.

[24] E. Björnson and L. Sanguinetti, "Power scaling laws and near-field behaviors of massive MIMO and intelligent reflecting surfaces," *IEEE Open J. Commun. Soc.*, vol. 1, pp. 1306–1324, Sep. 2020.

[25] A. de Jesus Torres, L. Sanguinetti, and E. Björnson, "Near-and far-field communications with large intelligent surfaces," in *Proc. 54th Asilomar Conference on Signals, Systems, and Computers*, 2020, pp. 564–568.

[26] E. Björnson, Ö. T. Demir, and L. Sanguinetti, "A primer on near-field beamforming for arrays and reconfigurable intelligent surfaces," in *Proc. 55th Asilomar Conference on Signals, Systems, and Computers*, 2021, pp. 105–112.

[27] A. Pizzo, L. Sanguinetti, and T. L. Marzetta, "Spatial characterization of electromagnetic random channels," *IEEE Open J. Commun. Soc.*, vol. 3, pp. 847–866, May 2022.

[28] L. Wei, C. Huang, G. C. Alexandropoulos, Z. Yang, J. Yang, W. E. Sha, M. Debbah, and C. Yuen, "Channel modeling and multi-user precoding for Tri-polarized holographic MIMO communications," *arXiv preprint arXiv:2302.05337*, 2023.

[29] N. Decarli and D. Dardari, "Communication modes with large intelligent surfaces in the near field," *IEEE Access*, vol. 9, pp. 165 648–165 666, Dec. 2021.

[30] H. Lu and Y. Zeng, "Communicating with extremely large-scale array/surface: Unified modelling and performance analysis," *IEEE Trans. Wireless Commun.*, vol. 21, no. 6, pp. 4039–4053, Jun. 2021.

[31] ——, "Near-field modeling and performance analysis for multi-user extremely large-scale MIMO communication," *IEEE Commun. Lett.*, vol. 26, no. 2, pp. 277–281, Feb. 2022.

[32] X. Li, H. Lu, Y. Zeng, S. Jin, and R. Zhang, "Near-field modeling and performance analysis of modular extremely large-scale array communications," *IEEE Commun. Lett.*, vol. 26, no. 7, pp. 1529–1533, Jul. 2022.

[33] ——, "Modular extremely large-scale array communication: Near-field modelling and performance analysis," *arXiv preprint arXiv:2208.05691*, 2022.

[34] S. Payami and F. Tufvesson, "Channel measurements and analysis for very large array systems at 2.6 GHz," in *Proc. 6th European Conference on Antennas and Propagation (EUCAP)*, 2012, pp. 433–437.

[35] Y. Han, S. Jin, C.-K. Wen, and X. Ma, "Channel estimation for extremely large-scale massive MIMO systems," *IEEE Wireless Commun. Lett.*, vol. 9, no. 5, pp. 633–637, May 2020.

[36] X. Li, S. Zhou, E. Björnson, and J. Wang, "Capacity analysis for spatially non-wide sense stationary uplink massive MIMO systems," *IEEE Trans. Wireless Commun.*, vol. 14, no. 12, pp. 7044–7056, Dec. 2015.

[37] A. Ali, E. De Carvalho, and R. W. Heath, "Linear receivers in non-stationary massive MIMO channels with visibility regions," *IEEE Wireless Commun. Lett.*, vol. 8, no. 3, pp. 885–888, Jun. 2019.

[38] X. Yang, F. Cao, M. Matthaiou, and S. Jin, "On the uplink transmission of extra-large scale massive MIMO systems," *IEEE Trans. Veh. Technol.*, vol. 69, no. 12, pp. 15 229–15 243, Dec. 2020.

[39] B. Xu, Z. Wang, H. Xiao, J. Zhang, B. Ai, and D. W. K. Ng, "Low-complexity precoding for extremely large-scale MIMO over non-stationary channels," *arXiv preprint arXiv:2302.00847*, 2023.

[40] A. Amiri, M. Angjelichinoski, E. De Carvalho, and R. W. Heath, "Extremely large aperture massive MIMO: Low complexity receiver architectures," in *Proc. IEEE Global Commun. Workshops (GC Wkshps)*, 2018, pp. 1–6.

[41] J. C. Marinello Filho, G. Brante, R. D. Souza, and T. Abrão, "Exploring the non-overlapping visibility regions in XL-MIMO random access and scheduling," *IEEE Trans. Wireless Commun.*, vol. 21, no. 8, pp. 6597–6610, Aug. 2022.

[42] O. S. Nishimura, J. C. Marinello, and T. Abrão, "A grant-based random access protocol in extra-large massive MIMO system," *IEEE Commun. Lett.*, vol. 24, no. 11, pp. 2478–2482, Nov. 2020.

[43] J. C. Marinello, T. Abrão, A. Amiri, E. De Carvalho, and P. Popovski, "Antenna selection for improving energy efficiency in XL-MIMO systems," *IEEE Trans. Veh. Tech.*, vol. 69, no. 11, pp. 13 305–13 318, Nov. 2020.

[44] A. Poon, R. Brodersen, and D. Tse, "Degrees of freedom in multiple-antenna channels: a signal space approach," *IEEE Trans. Inf. Theory*, vol. 51, no. 2, pp. 523–536, Feb. 2005.

[45] K. Zhi, C. Pan, H. Ren, K. K. Chai, and M. Elkashlan, "Active RIS versus passive RIS: Which is superior with the same power budget?" *IEEE Commun. Lett.*, vol. 26, no. 5, pp. 1150–1154, May 2022.

[46] T. Brown, P. Kyritsi, and E. De Carvalho, *Practical Guide to MIMO Radio Channel: With MATLAB Examples*. John Wiley & Sons, 2012.

[47] K. Zhi, C. Pan, H. Ren, K. Wang, M. Elkashlan, M. Di Renzo, R. Schober, H. Vincent Poor, J. Wang, and L. Hanzo, "Two-timescale design for reconfigurable intelligent surface-aided massive MIMO systems with imperfect CSI," *IEEE Trans. Inf. Theory*, early access, 2022.

[48] K. Zhi, C. Pan, H. Ren, and K. Wang, "Power scaling law analysis and phase shift optimization of RIS-aided massive MIMO systems with statistical CSI," *IEEE Trans. Commun.*, vol. 70, no. 5, pp. 3558–3574, May 2022.

[49] G. Interdonato, M. Karlsson, E. Björnson, and E. G. Larsson, "Local partial zero-forcing precoding for cell-free massive MIMO," *IEEE Trans. Wireless Commun.*, vol. 19, no. 7, pp. 4758–4774, Sep. 2020.

[50] K. Zhi, G. Chen, L. Qiu, X. Liang, and C. Ren, "Analysis and optimization of random cache in multi-antenna HetNets with interference nulling," in *Proc. IEEE Global Commun. Conf. (Globecom)*, 2019, pp. 1–6.

[51] L. Chang, W. Li, and W. Zhang, "Computing a near-maximum independent set in linear time by reducing-peeling," in *Proc. ACM International Conf. Management of Data*, 2017, pp. 1181–1196.

[52] I. S. Gradshteyn and I. M. Ryzhik, *Table of Integrals, Series, and Products*. Academic Press, 2014.